Electrowetting with Contact Line Pinning:
Computational Modeling and Comparisons with Experiments

Shawn W. Walker*

New York University, Department of Mathematics,
Courant Institute

Benjamin Shapiro†

University of Maryland, Bio-Engineering
and the Institute for Systems Research

Ricardo H. Nochetto‡

University of Maryland, Department of Mathematics
and the Institute for Physical Science and Technology

(Dated: August 31, 2009)

This work describes the modeling and simulation of planar electrowetting on dielectric (EWOD) devices that move fluid droplets by modulating surface tension effects. The fluid dynamics are modeled by Hele-Shaw type equations with a focus on including the relevant boundary phenomena. Specifically, we include contact angle saturation and a contact line force threshold model that can account for hysteresis and pinning effects. These extra boundary effects are needed to make reasonable predictions of the correct shape and time scale of liquid motion. Without them the simulations can predict droplet motion that is much faster than in experiments (up to 10-20 times faster). We present a variational method for our model, and a corresponding finite element discretization, that is able to handle surface tension, conservation of mass, and the non-linear contact line pinning in a straightforward and numerically robust way. In particular, the contact line pinning is captured by a variational inequality. We note that all the parameters in our model are derived from first principles or from independent experiments except one (the parameter D_{visc} that accounts for the extra resistive effect of contact angle hysteresis and is difficult to measure directly). We quantitatively compare our simulation to available experimental data for five different cases of droplet motion that include splitting and joining of droplets and find good agreement with experiments.

PACS numbers: Valid PACS appear here

I. INTRODUCTION

Electrowetting refers to the local modification of surface tension by applied electric actuation to precisely manipulate 2-phase flows on the micro-scale[1–15]. By applying electric fields via actuating electrodes (see Figure 1), surface tension and electrical effects compete[5,16,17], and this competition can create spatially and temporally varying forces that are used to shape, move, split, merge, and mix fluids in micro-scale devices. Applications of electrowetting include reprogrammable lab-on-a-chip systems[4,11], auto-focus cell phone lenses[1], and colored oil pixels for laptops and video-speed smart paper[3,9,10].

This paper is concerned with modeling and simulating fluid motion in planar electrowetting on dielectric (EWOD) systems, such as the UCLA electrowetting system[2,17–19] against which the numerical results in this paper are compared. It focuses on device length (μm) and device time scale (ms) simulations and it addresses the next major item required to better predict electrowetting behavior: the inclusion of contact line pinning and de-pinning behavior in a experimentally motivated phenomenological and *numerically sound* manner.

The subject of this paper, modeling and simulation

of electrowetting, is needed to further understand the physics and to design, optimize, and better control next generation devices. For instance, our results on feedback flow control to steer and sort single particles in planar electrowetting systems, a new capability for electrowetting[20], was predicated on and would not have been possible without our prior electrowetting modeling work[21]. Modeling for design and control must strike a balance between model accuracy (the model must sufficiently predict the experimental behavior) and model complexity. To enable design, optimization, and control, the models created must be small enough to fit within design, optimization, and control tools, e.g. control analysis and synthesis methods[22,23] which can handle tens to tens of thousands of states, but not millions.

Effectively modeling electrowetting at device length and time scales is challenging. Electrowetting includes a complex set of physical phenomena, and aspects related to fine-scale fluid dynamics and chemistry are still under debate in the literature. Nevertheless, the key modeling issues and necessary tasks have become clear (see, for example, our previous work[17,21,24–26] and the review[5]). The following are crucial and recognized modeling issues that must be included.

1. In electrowetting, liquid packets are held together by surface tension and are actuated by electric fields, so any model must include surface tension and electrical
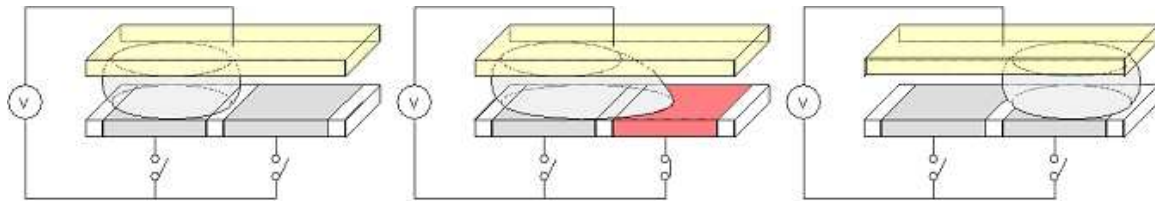
FIG. 1: An example of electrowetting (schematic). The activated electrode (red pad) effectively and locally decreases the surface tension of the liquid touching it, causing it to move to the right. (Figure courtesy Jeong-Yeal Yoon at UCLA.)

phenomena.

2. For fast motion, which certainly occurs in electrowetting systems (millisecond splitting of droplets, video-speed actuation of colored oils), fluid *dynamic* effects must be included.

3. Liquid/gas interfaces must be tracked accurately and successfully through large deformations including topological changes such as split and join events. Such events are central to the operation of laboratory-on-a-chip electrowetting systems that aim to manipulate, combine, and partition small packets of liquid to carry out precision chemical and biological reactions on chip.

4. Loss mechanisms, such as contact angle saturation[2,17,18,27–37] and hysteresis[38–47], which are two major phenomena in electrowetting systems, can severely limit device performance and must be included.

The current status of electrowetting physical modeling can be summarized as follows. We know the dominant physics that must be included to characterize the bulk flow. Equilibrium behavior, of sessile (isolated) drops is understood[16,17,33,40,48]. The bulk fluid *dynamics* of electrowetting has been addressed by us as well as by others. Our prior work[21] developed a model in 2 dimensions that successfully tracked moving and splitting interfaces by the level-set method and, to the best of our knowledge, was the first to predict electrowetting dynamics from physical first principles (see also Lu et al's model[34]). We compared that model[21] to the UCLA experiments and showed that it captures the leading order effects (i.e. it is quantitatively correct in most cases, for example, it correctly predicts bulk flow splitting times).

Numerical advances for tracking the dynamic 2-phase micro-scale flows that occur in electrowetting devices include our prior research in[21,25,26], as well as the results of others[34,49–52]. Earlier work on electrowetting focused mainly on equilibrium and quasi-static behavior of droplets[49,50] (i.e. no internal fluid dynamics). More recent methods simulate the full dynamics of electrowetting driven motion in various physical settings[34,51,52]. However, none of these methods/models account for the effects of contact line pinning or hysteresis. It is also not apparent how to generalize the above listed numerical techniques to include these two phenomena.

In summary, this paper presents a PDE model of EWOD fluid dynamics that is able to approximately capture the evolution of the fluid's liquid-gas interface in two dimensions. In our prior modeling work we had correctly accounted for the internal fluid dynamics, the boundary conditions due to surface tension and electrowetting actuation, but we had only a heuristic model for contact line pinning and hysteresis[21]. Now we include a phenomenological force threshold model for line-pinning and de-pinning as motivated by the experiments described in[5,41,53]. It is simply not feasible to include atomistic or molecular dynamic descriptions for contact line dynamics explicitly as their length and time scales are dramatically smaller (i.e. 10,000 and 100 times smaller than device length and time scales respectively), but we do include insights from them in our formulation (see Section II D and[54–57]). We combine sophisticated numerics, a semi-implicit front-tracking method for the interface motion and a variational/weak formulation of the governing PDE, which we discretize by finite elements[25]. The variational method is key to implementing our contact line pinning model in a clean and robust manner, as well as providing a stable calculation of curvature, and ensuring accurate mass conservation. Our simulation tool is able to handle pinching and merging of droplets[26], which is central to the operation of electrowetting systems. Our simulations with the added contact line physics and new numerical methods provide a better match to experimental data than those in[21,34,52] and they still run in between 5 and 15 minutes on a laptop. We show direct comparison between our simulation and experiments conducted at UCLA in Section IV.

II. ELECTROWETTING MODEL

This section describes our modeling approach. A list of physical parameters for the device geometry and other symbols used in the text are given in Table I.

A. Description of the EWOD System

Figure 2 shows a schematic of an EWOD device. EWOD actuation relies on a competition between surface tension and dielectric energy storage in an underlying solid dielectric layer[5,17]. This effectively allows each electrode to change the surface tension properties immediately above it. This change can be used to move droplets from electrode to electrode, to split droplets (by pulling on either side using three electrodes), to join droplets
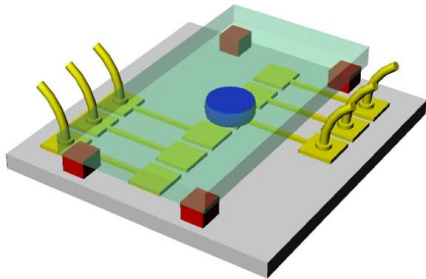
FIG. 2: Schematic of sample EWOD device (courtesy of CJ Kim at UCLA). This EWOD system consists of two parallel plates with the top plate (transparent) acting as a ground electrode and the bottom plate containing a grid of embedded electrodes. The bottom plate also contains an extra dielectric layer to enhance device performance (not shown). A single droplet is shown in blue, but there may be many droplets of arbitrary shape between the two plates. Note that the height of each droplet is small compared to its horizontal size (these droplets are very thin puddles).

by making them collide, and to mix fluid in droplets by making the droplets execute complex paths.

B. Base Fluid Model

1. Hele-Shaw

The flow of liquid between two narrowly spaced parallel plates, surrounded by air, is governed by the Hele-Shaw equations[58,59], with a pressure boundary condition given by the Young-Laplace relation at the liquid-gas interface. Therefore, the 2 dimensional fluid equations inside (possibly many) droplets actuated by EWOD are given in non-dimensional form as (see[21,25] for details)

$$\alpha \frac{\partial \mathbf{u}}{\partial t} + \beta \mathbf{u} + \nabla p = 0, \text{ in } \Omega,$$
$$-\nabla^2 p = 0, \text{ in } \Omega, \tag{1}$$

where Ω is the domain of the fluid (liquid-phase, see Figure 3), bold-face $\mathbf{u}$ is the vector velocity field (in the plane of the device), and p is the pressure. The non-dimensional constants α and β depend on the fluid parameters and geometry of the device:

$$\alpha = \left(\frac{\rho L U_0}{\mu} \right) \text{Ca}, \quad \beta = 12 \left(\frac{L}{H} \right)^2 \text{Ca}, \quad \text{Ca} = \frac{\mu U_0}{\sigma_{\text{lg}}},$$

where ρ is fluid density, H is the height between the parallel plates, L is the planar liquid length scale, U_0 is the velocity scale, μ is the dynamic viscosity, Ca is the capillary number, and σ_{lg} is the surface tension of the liquid-gas interface (here denoted by Γ)[21].
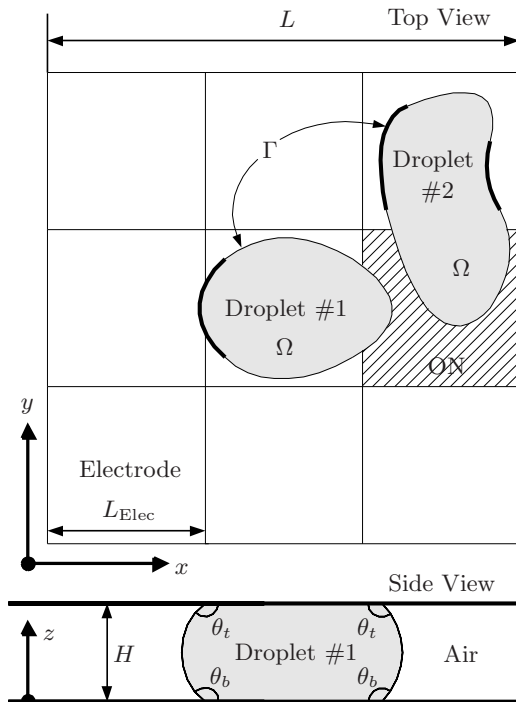

FIG. 3: Example EWOD device geometry (see[2]). The coordinate axes are defined such that the top and bottom plates of the device lie in planes parallel to the x-y plane. In this example, a 3x3 grid of electrodes is shown, each with side length L_{Elec}, with one electrode active (the shaded square). Two liquid droplets are shown moving towards the active electrode to merge into one droplet. The domain of the liquid is denoted by Ω and the liquid-gas interface is labeled Γ. The bolded parts of Γ indicate 'pinned' parts of the boundary due to contact line pinning. Note that only a subset of the boundary may be pinned; other parts may still move. A side view of the device is shown at the bottom (note: 'Droplet #2' is not shown here). The contact angles of the droplet, measured through the liquid, are denoted θ_t and θ_b (top and bottom). The physical parameters of the device, for each experimental setup, are listed in Tables I and III.

2. Interface Motion

We need an equation to describe the motion of the two-phase droplet boundary Γ. In particular, the droplet may deform into an arbitrary shape. The change in droplet shape is only due to the normal component of velocity $\mathbf{u} \cdot \mathbf{n}$; the tangential component only reparametrizes the interface. Thus, for each point $\mathbf{x}$ on the boundary the change in position is given by

$$\partial_t \mathbf{x} = \left(\mathbf{u}(\mathbf{x}, t) \cdot \mathbf{n}(\mathbf{x}, t) \right) \mathbf{n}(\mathbf{x}, t), \tag{2}$$

where $\mathbf{n}$ is the unit outer normal vector of the boundary. However, it is convenient in our implementation to use the full velocity to advance the interface position:

$$\partial_t \mathbf{x} = \mathbf{u}(\mathbf{x}, t). \tag{3}$$

This makes no difference for the droplet evolution and simplifies our numerical method. In the numerical imple-

TABLE I: Nomenclature: List of important symbols used in the text. The physical parameters of the UCLA EWOD device for the experiments described in Section IV are given in Table III.

Parameter	Symbol Definition
Surface Tension	σ_{lg}
Dynamic Viscosity	μ
Density	ρ
Channel Height	H
Electrode Length	L_{Elec}
Length Scale	L
Velocity Scale	U_0
Time Scale	$t_0 = L/U_0$
Pressure Scale	$P_0 = \sigma_{\mathrm{lg}}/L$
Reynolds Number	$\mathrm{Re} = \rho U_0 H/\mu$
Capillary Number	$\mathrm{Ca} = \mu U_0/\sigma_{\mathrm{lg}}$
Momentum Equation Coefficients	$\alpha,\ \beta$
Vector Velocity	$\mathbf{u}$
Pressure	p
Pinning Variable	λ
Convex Set (for λ)	Λ
Curvature of Γ	κ
Unit Normal and Tangent Vectors of Γ	$\mathbf{n},\ \mathbf{t}$
EWOD Force	E
Maximum Pinning Pressure	P_{pin}
Viscous Interface Drag	D_{visc}
Numerical Time Step	δt
2-D Fluid Domain	Ω
1-D Liquid-Gas Interface	Γ
Surface Gradient Operator	∇_Γ
Laplace-Beltrami Operator	Δ_Γ

mentation of our model (see Section III F), we have an explicit representation of the liquid domain Ω by a mesh of triangles. This naturally contains a mesh of the liquid-gas interface Γ (i.e. the boundary of Ω), which allows for easily enforcing boundary conditions and computing surface tension forces (see Section III). Hence, our method falls into the category of semi-implicit front-tracking.

C. Boundary Conditions for the Liquid

We now discuss the physical phenomena occurring at the liquid-gas interface, how these effects are modeled and how they affect the boundary conditions.

1. Surface Tension

We first review the pressure boundary conditions for pure surface tension driven flow, and then show how electrowetting actuation is introduced (details are given in our prior paper[21]).

The Young-Laplace relation[59] for the pressure in (1) gives the boundary condition on the liquid-gas interface Γ in dimensional form (denoted by $\tilde{\ }$):

$$\tilde{p} = \sigma_{\mathrm{lg}}(\tilde{\kappa}_1 + \tilde{\kappa}_2),\ \text{on } \Gamma, \tag{4}$$

where $\tilde{\kappa}_1$, $\tilde{\kappa}_2$ are the principle curvatures[60] of the 2 dimensional liquid-gas surface. Following[21], the principle directions of curvature are taken to be orthogonal, with one direction in the plane of the device and the other along the channel height. Therefore, the boundary condition can be decomposed as:

$$\tilde{p} = \sigma_{\mathrm{lg}}(\tilde{\kappa} + \tilde{\kappa}_z),\ \text{on } \Gamma, \tag{5}$$

where $\tilde{\kappa}$ is the curvature in the plane of the device and $\tilde{\kappa}_z$ is along the height. Since our fluid model is in 2 dimensions, we have no information on the liquid-gas interface shape along the channel height. Ergo, we assume that $\tilde{\kappa}$ only depends on the shape of the 1 dimensional boundary Γ, and we estimate $\tilde{\kappa}_z$ by assuming the liquid-gas interface profile is circular along the channel height. This is a reasonable assumption so long as the horizontal extent of the droplet is large compared to the height of the EWOD device. This is certainly the case in the UCLA devices where droplets usually span at least one electrode (1.4-1.5 mm length) while the device height is 70-100 μm. Then knowing the contact angles that the droplet makes with the top and bottom plates, at each point $\mathbf{x}$ on Γ, fully determines $\tilde{\kappa}_z$ as a function on Γ[21]. The contact angle only depends on a local force balance[61,62], so it does not depend on the channel height. Therefore, $\tilde{\kappa}_z = \kappa_z/H$ where κ_z is the non-dimensional z curvature given by:

$$\kappa_z = -(\cos(\theta_t) + \cos(\theta_b)),\ \text{on } \Gamma, \tag{6}$$

where θ_t and θ_b are the top and bottom contact angles (see Figure 3). The dimensional curvature of Γ is given by $\tilde{\kappa} = \kappa/L$, where κ is non-dimensional. Hence, the non-dimensional pressure is given by

$$p = \kappa + \frac{L}{H}\kappa_z,\ \text{on } \Gamma, \tag{7}$$

where $p = \tilde{p}/P_0$ and $P_0 = \sigma_{\mathrm{lg}}/L$ is the pressure scale.

2. EWOD Forcing

The contact angle of the liquid (on the bottom plate) depends on the voltage of the electrode pad directly underneath (see Figure 3). Meaning the contact angle at a point $\mathbf{x}$, on the interface Γ, only depends on the electrode voltage at position $\mathbf{x}$[17], i.e. $\theta_b(\mathbf{x}) = \theta_b(\mathrm{V}(\mathbf{x}))$. Hence, $\kappa_z(\mathbf{x}) = \kappa_z(\mathrm{V}(\mathbf{x}))$ is voltage dependent.

Let E be the EWOD force coming from the z curvature component of the Laplace pressure on the interface. The above implies

$$E(\mathbf{x}) := \frac{L}{H}\kappa_z(\mathrm{V}(\mathbf{x})), \tag{8}$$

which rewrites (7) as

$$p = \kappa + E,\ \text{on } \Gamma. \tag{9}$$

Computing E requires evaluating the voltage in the plane of the device. In our model, the voltage $\mathrm{V}(\mathbf{x})$ is interpolated between electrode gaps to ensure a smooth variation of the bottom contact angle along the interface Γ.

TABLE II: Available contact angle versus voltage data for the experiments in Sections IV A, IV D, and IV E.

Voltage (V)	Contact Angle (degrees)	
	Glycerin[a]	Water[b]
0	107.35	111.62
50	68.46	-[c]
65	64.32	70.01

[a]Used in Sections IV A and IV D.
[b]Used in Section IV E.
[c]This data is not needed.

3. Contact Angle versus Voltage; Saturation

The initial model of contact angle variations versus voltage is the Young-Lippmann equation[27], which predicts a parabolic curve relating contact angle to the capacitive voltage V across the bottom plate (see Figure 4), i.e.

$$\cos\theta = \frac{\sigma_{\mathrm{sg}} - \sigma_{\mathrm{sl}} + C_{\mathrm{cap}}V^2/2}{\sigma_{\mathrm{lg}}}, \qquad (10)$$

where θ is the contact angle, σ_{sg} and σ_{sl} are the surface tensions of the solid-gas and solid-liquid layers (respectively), and C_{cap} is the capacitance per unit area for the charging layer underneath the electrode. However, in real electrowetting applications there are loss mechanisms that lead to contact angle saturation[2,17,18,27–37]. These limit the amount of contact angle variation (i.e. $\Delta\theta_b$) that can be actuated, which in turn limits the range of values of the EWOD forcing E. If the Young-Lippmann model is used, simulated droplet speeds far exceed what is actually seen in experiments[21]. The saturation effect is subtle and non-obvious, and its root causes are the subject of vigorous debate in the electrowetting community. See the previous references for more information on contact angle saturation.

In Figure 4, we show a contact angle versus voltage curve for a particular type of EWOD device[2]. The solid curve is used in our simulations and comparisons to experiments in Sections IV B and IV C. The moving droplet experiment in Section IV B has a voltage time sequence with values ranging from 0V to 25V; hence, here we require the entire fitted solid curve in Figure 4. As for the experiments shown in Sections IV A, IV D, and IV E we only need the experimental contact angle versus voltage data given in Table II; no intermediate voltages are applied in those experiments.

D. Contact Line Force Threshold Model

Contact line pinning (or sticking) is a readily observed phenomenon in most wetting applications[38–44,63–69]. It is not a fluid viscous effect but rather a kind of molecular adhesion that occurs at the three-phase contact line of the droplet. Line pinning is also related to an effect
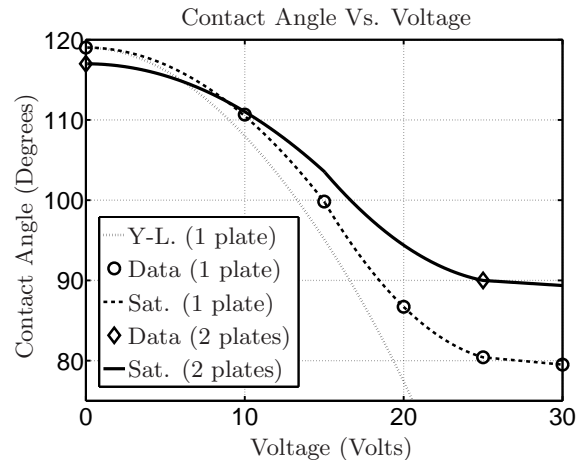

FIG. 4: Contact angle versus voltage data: theoretical and experimental data for contact angle variations using electrowetting on dielectric. The light dotted line denoting the Young-Lippmann (Y-L) curve is theoretical[27,32,33]. The single plate saturation curve has six experimental data points (given in[2]) with a piecewise interpolating polynomial (see dashed line and '∘' data points). The two plate saturation curve has two experimental data points (also from[2]) with an interpolating curve derived from the single plate case by using a linear map[21] (see solid line and '⋄' data points). Note the 'saturation' effect as the voltage increases. The solid curve is used in computing the pressure boundary conditions, via equations (6), (8), and (9). Specifically, this data is used in simulating the experiments in Sections IV B and IV C. If the Young-Lippmann curve was used, then the simulated droplet speed would be significantly higher than in experiment[21] (figure reproduced from[21]).

called contact angle hysteresis which acts to retard interface motion. Ignoring pinning and hysteresis leads to simulations that predict droplet motion up to 10 times faster than is seen in experiments[21].

As of today, the nature of pinning and hysteresis is still controversial. Most modeling of contact line pinning uses molecular dynamics simulations[65–68], which are computationally very expensive (state-of-the-art simulations are restricted to $\approx 10^4$ atoms, and/or nanometer length scales and (at best) nanosecond time periods). The following sections describe a modification of the pressure boundary conditions to account for both contact line pinning and the retardation effect of hysteresis in a physically meaningful way. This is in contrast to our prior work[21], which had no pinning model and used an ad-hoc model of contact angle hysteresis.

1. Phenomenological Approach

Macroscopic experiments[5,41,53] of droplet motion on an inclined plane indicate that the net line pinning force acting on a droplet has a threshold value. In other words, the contact line exerts a force, equal and opposite to a body force (e.g. gravity), that prevents the droplet from moving, but only up to a threshold value. If the body

force exceeds the threshold, then motion does occur. This behavior is very reminiscent of mechanical (Coulombic) friction, in which case the friction force always opposes motion and cannot exceed a certain threshold value. It was also found[5,41] that the maximum total pinning forces on the droplet scales with the length of the contact line, i.e.

$$F_{\max} = c_{\mathrm{pin}} L_{\mathrm{cl}}, \tag{11}$$

where $F_{\max}$ is the maximum total force that can resist motion of the droplet, L_{cl} is the total contact line length, and c_{pin} is the line pinning coefficient with units of force per length (units of surface tension). So the constant c_{pin} represents the maximum force per unit length that a piece of contact line can exert against the droplet to prevent its motion. In view of equation (11), we model line pinning as a *local* effect, meaning that a local piece of contact line only resists the local motion of that portion of the liquid-gas interface, but will assume that the maximum threshold force on that piece of contact line cannot exceed its length times the coefficient c_{pin}. For our setup, this is achieved by modifying the pressure boundary conditions (see Section II D 2 for more details).

Our model is a rough approximation of the actual physics at the three-phase contact line, but it does capture some insights from fine scale modeling of interfaces, such as in[54–57], on moving contact lines. In particular,[54] shows a discontinuous jump in the local applied force versus local interface velocity. The essential contribution of our work is to develop a modeling and numerical framework that will allow inclusion of such results into electrowetting modeling of entire devices for design and optimization. To do this it is necessary to use a phenomenological approach to incorporate the pinning effect into our continuum model. This is done to avoid a molecular/atomistic description. Recently[62,70,71], some new models for contact line dynamics have been proposed that avoid a purely atomistic description and are designed to be incorporated into a continuum model; these also make note of insights from molecular dynamics. As noted by us and others, it is clearly desirable to have tractable contact line models at device/system length and time scales.

2. Including Line Pinning into the Governing Equations

Since the EWOD governing equations are posed in 2 dimensions, we must average the above line force threshold model over the device height in order to incorporate it into the pressure boundary conditions. This is done by averaging the maximal line pinning coefficient c_{pin} over the channel height H of the EWOD device (see Figure 5). This gives a maximal 'pinning pressure' $\widetilde{P}_{\mathrm{pin}} = 2c_{\mathrm{pin}}/H$ (in dimensional form), which represents the maximum opposing force per liquid-gas interface area that the contact line can apply *against* motion of the interface. The factor of '2' accounts for the interface contact line pinning at the floor and ceiling of the EWOD device. The
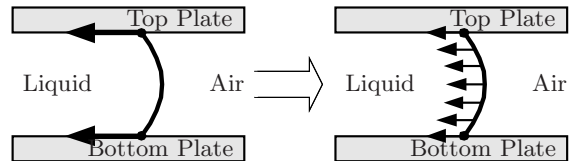

FIG. 5: Contact line force averaging (cross-sectional slice of EWOD device shown; z-axis is in the vertical direction). Contact line friction is a force that is active along the three-phase contact line. On the left, the contact line pinning force is shown concentrated at the contact line (at both the floor and ceiling). On the right, the pinning force has been redistributed over the channel height. Since the governing EWOD fluid equations have been averaged along the channel height, we average the contact line pinning force across the channel height also. This redistributes the force from a length of contact line (at floor and ceiling) to a vertical strip along the liquid-gas interface. This allows the line pinning force to be included in the pressure boundary conditions as an additional pressure term (see equation (13)).

non-dimensional pinning pressure is then given by

$$P_{\mathrm{pin}} = \frac{1}{P_0} \frac{2c_{\mathrm{pin}}}{H}, \tag{12}$$

where P_0 is the dimensional reference pressure scale (force per unit of area).

This allows us to introduce a locally defined pinning pressure λ into the boundary conditions (in non-dimensional form)

$$\begin{aligned} p &= \kappa + E + \lambda, \\ \lambda &= P_{\mathrm{pin}} \, \mathrm{sgn}(\mathbf{u} \cdot \mathbf{n}) \end{aligned} \tag{13}$$

In other words, if the normal velocity of the liquid-gas interface is positive, then the pinning pressure will push back with maximum positive pressure $+P_{\mathrm{pin}}$ to limit the motion. Likewise, if the normal velocity is negative, the pinning pressure will push back in the opposite direction $-P_{\mathrm{pin}}$. And if the normal velocity is zero, then λ takes on a value between $\pm P_{\mathrm{pin}}$ and acts as a Lagrange multiplier to enforce the constraint that the interface does not move (also see Figure 6). This definition of λ ensures $|\lambda| \leq P_{\mathrm{pin}}$ and so is consistent with the experimental observation in Section II D 1.

Numerical implementation of this simple phenomenological model is difficult because of the discontinuity (the sign function of equation (13), see Figure 7). This discontinuity, however, is essential. If it was replaced by a smooth function then no droplet could ever be pinned in a non-circular shape, something that *does* occur in the experiments (see Figure 14). To show this, we argue by contradiction. Assume no EWOD forcing, so the boundary pressure is given by $p = \kappa + \lambda$ (from equation (13)). Suppose the droplet has become completely pinned in a non-circular shape but the function relating λ to the normal front velocity $\mathbf{u} \cdot \mathbf{n}$ is smooth. Any symmetric smoothed version f of the sign function 'sgn' must have $\lambda = P_{\mathrm{pin}} f(0) = 0$, which implies $p = \kappa$ by equation (13).
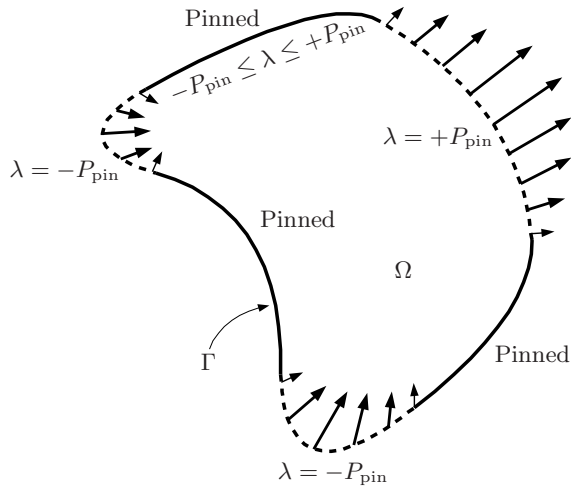
FIG. 6: A 2 dimensional droplet (top view) with parts of the boundary pinned (electrode grid not shown). The pinned regions are denoted by a solid line; unpinned regions are shown as a dashed line with velocity arrows indicating direction of motion. An outward motion is considered positive ($\mathbf{u} \cdot \mathbf{n} > 0$), and an inward motion is negative ($\mathbf{u} \cdot \mathbf{n} < 0$). The pinning variable λ is defined on the boundary Γ of the droplet. On the unpinned regions, the value of λ saturates to $\pm P_{\mathrm{pin}}$. On the pinned regions ($\mathbf{u} \cdot \mathbf{n} = 0$), λ varies between $-P_{\mathrm{pin}}$ and $+P_{\mathrm{pin}}$ (see Figure 7). In our simulations, $|\lambda| < P_{\mathrm{pin}}$ is used to indicate where the boundary is pinned.

But if the droplet is pinned in a non-circular shape, then κ will not be constant around the droplets circumference, hence the pressure field inside the droplet will not be constant[72]. By equation (1), the velocity $\mathbf{u}$ will not be zero which contradicts the droplet being pinned. Note that a smooth but steep function f will lead to a slowly creeping liquid, but only a discontinuous f can truly pin the liquid. Moreover, our model with the sgn function is a physically motivated description[5,38–44,63–68].

Our model, with equation (13), is non-linear and introduces the velocity into the pressure boundary conditions. Moreover, it is local, meaning that multiple parts of the boundary Γ can be pinned and unpinned simultaneously. Furthermore, the regions where the droplet is pinned/unpinned are not known a priori; this must be determined as part of the solution. Our pinning model is similar to the Signorini problem in elasticity[73] which models the deformation of an elastic body against a rigid obstacle and utilizes a contact variable to enforce the rigid constraint similarly to our λ. Our model can be increased in complexity (see Section II D 3) to account for more interesting contact line dynamics[54–57]. We are able to include this model into our variational formulation of Section III, and we have a method of solving for the velocity, pressure, and λ[25,74]. Knowing λ immediately yields where the boundary is pinned/unpinned.

One important issue here is the three-phase line singularity[75–77], which originates because of an apparent paradox between the no-slip boundary condition on the walls of the device and the fact that the contact line
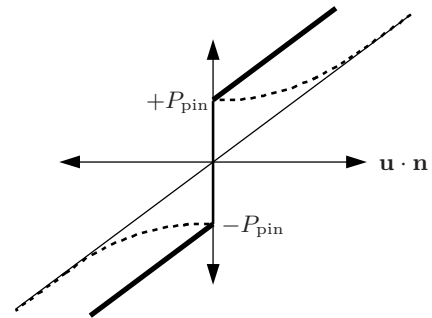

FIG. 7: A more realistic relationship between the resistive pressure at the interface and the normal velocity. Here, $[\lambda + D_{\mathrm{visc}}\mathbf{u} \cdot \mathbf{n}]$ is plotted as the thick line. Note how the interface pressure increases with increasing velocity. The dashed line depicts a slightly more non-linear relationship $[\lambda + D_{\mathrm{visc}}\mathbf{u} \cdot \mathbf{n} + G_{\mathrm{fric}}(\mathbf{u} \cdot \mathbf{n})]$ (see equation (16)). The qualitative form of the dashed line has been shown in the work of[54–57]. Note: the dashed line asymptotes towards the thin line $D_{\mathrm{visc}}\mathbf{u} \cdot \mathbf{n}$.

moves. Our formulation is only a 2 dimensional description, as appropriate for planar devices. We do not track the location of the three-phase line in our model in 3 dimensions; we only have an 'averaged' description of the liquid-gas interface. Recall that the velocity field in the z direction is parabolic; a fundamental assumption in Hele-Shaw flow. Thus, in our model the contact line singularity is not present. Other explanations have been posed recently that resolve the paradox and imply that there is no singularity[62,67,68,70,71].

3. Including Hysteresis Into Contact Line Dynamics

Our model can be extended to include more interesting contact line dynamics. Contact angle hysteresis, which refers to the difference in contact angles between the advancing and receding fronts, acts as an additional type of resistance to interface motion[21]. It is a direct consequence of contact line pinning, and can be seen when water droplets stick to the side of a solid surface. For more information see[38–44].

The main effect of contact angle hysteresis is to limit the speed of motion of droplets moving on substrates. If only contact line pinning is assumed, with experimentally measured values for c_{pin}, then our model predicts EWOD driven droplet motion up to 10 times faster than in experiment[21]. In our prior work[21], this was compensated by introducing an ad-hoc 'hysteresis constant'.

In the present paper, we can account for hysteresis by adding another term to the pressure boundary conditions

$$p = \kappa + E + \lambda + D_{\mathrm{visc}}\mathbf{u} \cdot \mathbf{n}, \qquad (14)$$

where $D_{\mathrm{visc}} > 0$ is a constant. The $D_{\mathrm{visc}}\mathbf{u} \cdot \mathbf{n}$ term is a straightforward modification of the interface force threshold model in the previous section (see Figure 7). Increasing D_{visc} locally reduces the speed of droplet interface motion. This can account for the extra resistive

effect of contact angle hysteresis. Moreover, we can modify the linear term to be slightly non-linear, e.g.

$$p = \kappa + E + [\lambda + D_{\text{visc}}\mathbf{u} \cdot \mathbf{n} + G_{\text{fric}}(\mathbf{u} \cdot \mathbf{n})], \qquad (15)$$

where, for example, G_{fric} is a monotone decreasing function:

$$G_{\text{fric}}(\mathbf{u} \cdot \mathbf{n}) := -\frac{P_{\text{pin}}}{\pi/2} \arctan\left(\frac{D_{\text{visc}}}{P_{\text{pin}}/\frac{\pi}{2}}\mathbf{u} \cdot \mathbf{n}\right) \qquad (16)$$

This type of force versus velocity relationship for contact line motion can incorporate insights from atomistic or molecular dynamic studies, such as in the work of[54–57]. It introduces a 'damping' effect that retards local interface motion. Choosing D_{visc} properly captures the correct time-scale of interface motion. This is the *only* fitting parameter in our model; the value of c_{pin} for the line pinning was obtained independently through an in-house inclined plane droplet experiment (see Table III). We emphasize that available data for c_{pin} and D_{visc} is not readily available in the literature.

E.   Final Equation Summary

We rewrite the governing equations in an equivalent form, which will be convenient for our numerical implementation:

$$\alpha\partial_t\mathbf{u} + \beta\mathbf{u} + \nabla p = 0, \quad \text{in } \Omega,$$
$$\nabla \cdot \mathbf{u} = 0, \quad \text{in } \Omega, \qquad (17)$$
$$p\mathbf{n} - \kappa\mathbf{n} - \lambda\mathbf{n} - D_{\text{visc}}(\mathbf{u} \cdot \mathbf{n})\mathbf{n} = E\mathbf{n}, \text{ on } \Gamma,$$

where the first equation is conservation of momentum and the second is conservation of mass; E is the electrowetting forcing from Section II C 2. The third equation is the pressure boundary condition multiplied by the outward pointing unit normal vector $\mathbf{n}$; this will be useful in the next section. For simplicity, we omit the extra G_{fric} term. As noted previously, the pinning variable λ is defined by

$$\lambda = P_{\text{pin}} \text{sgn}(\mathbf{u} \cdot \mathbf{n}), \text{ on } \Gamma. \qquad (18)$$

Note that Laplace's equation for pressure (see equation (1)) has been replaced by the second equation in (17) (incompressibility)[78]. The equations in (17) are more convenient because they give rise to a mixed variational formulation of the PDE model that allows the pressure boundary condition to be included as a natural boundary condition, which permits computing the curvature κ implicitly (see Section III B). Lastly, we recall the interface motion equation (3) from Section II B 2:

$$\partial_t\mathbf{x} = \mathbf{u}(\mathbf{x}, t), \text{ on } \Gamma. \qquad (19)$$

III.   VARIATIONAL FORMULATION

We present a time-discretization of the EWOD fluid equations with contact line pinning followed by a variational formulation of the governing PDE. Variational

forms appear in elasticity under the name of virtual displacements. They are standard[72] and allow the use of finite element methods[79,80] which are among the most efficient, flexible, and accurate numerical techniques in science and engineering for solving PDEs.

A.   Time-Discrete EWOD Equations

Next, we derive the time-discrete version of (17) and (19) by first partitioning the time axis into time-steps δt_i, for i in some finite index set. Let Ω^i and Γ^i be the fluid domain and liquid-gas interface at time t_i, respectively (see Figures 3 and 6, and the nomenclature in Table I). Then the semi-implicit, time-discrete version of (17) is listed as

$$\alpha\frac{\mathbf{u}^{i+1} - \mathbf{u}^i}{\delta t_{i+1}} + \beta\mathbf{u}^{i+1} + \nabla p^{i+1} = 0, \qquad \text{in } \Omega^i,$$
$$\nabla \cdot \mathbf{u}^{i+1} = 0, \qquad \text{in } \Omega^i, \quad (20)$$
$$p^{i+1}\mathbf{n}^i - \kappa^{i+1}\mathbf{n}^i - \lambda^{i+1}\mathbf{n}^i$$
$$-D_{\text{visc}}(\mathbf{u}^{i+1} \cdot \mathbf{n}^i)\mathbf{n}^i = E^i\mathbf{n}^i, \text{ on } \Gamma^i,$$

where $\mathbf{u}^i$ is the (known) vector velocity at time index t_i, and $\mathbf{n}^i$ is the outward pointing normal vector of Γ^i. Here, we have used a backward Euler finite difference approximation of the time derivative term $\partial_t\mathbf{u}$. The geometry is kept explicit in (20) and the solution variables $(\mathbf{u}^{i+1}, p^{i+1}, \lambda^{i+1})$ are implicit. The curvature κ^{i+1} is an approximation of the curvature of Γ^{i+1} and is treated semi-implicitly (see Section III B).

Treating the solution variables implicitly while keeping the domain explicit is called a *semi-implicit* method. We chose this because it is more convenient to compute on the current domain Ω^i than the future unknown domain Ω^{i+1}. If there is no pinning (i.e. $\lambda = 0$), then it leads to a linear set of equations that describes the velocity and pressure at each time-step. This is useful in our iterative method when solving the system with pinning $\lambda \neq 0$ (see Section III F). Keeping the solution variables implicit ensures numerical stability, while avoiding an unnecessarily small time-step[81,82]. This is especially true for the curvature[83–85].

Now we can approximate how a point on the interface moves using a time-discrete version of (19):

$$\mathbf{x}^{i+1} := \mathbf{x}^i + \delta t_{i+1}\mathbf{u}^{i+1}(\mathbf{x}^i), \qquad (21)$$

where $\mathbf{u}^{i+1}$ is the velocity (defined on Ω^i) at the next time index, $\mathbf{x}^i$ is a point on Γ^i, and $\mathbf{x}^{i+1}$ is the corresponding point on Γ^{i+1}.

B.   Implicit Curvature Calculation

The curvature κ^{i+1} is treated in an implicit way to avoid an unnecessarily small time-step restriction to guarantee stability[83]. In the following, we show how to discretize (in time) the vector curvature $\kappa^{i+1}\mathbf{n}^i$.

First, we briefly review some differential geometry[60,86,87]. The 'surface gradient' on a surface Γ is denoted ∇_Γ and is a vector operator. If Γ is a 1 dimensional curve, $\nabla_\Gamma = \mathbf{t}\partial_s$ (i.e. ∂_s is the derivative with respect to arc-length, $\mathbf{t}$ is the unit tangent vector). The Laplace-Beltrami operator or 'surface Laplacian' is defined as $\Delta_\Gamma = \nabla_\Gamma \cdot \nabla_\Gamma$, and is just the second derivative with respect to arc-length in the case of a 1 dimensional curve. The vector curvature $\boldsymbol{\kappa}^i = \kappa^i \mathbf{n}^i$ of Γ^i satisfies

$$\boldsymbol{\kappa}^i = -\Delta_{\Gamma^i}\mathbf{x}^i, \tag{22}$$

treating $\mathbf{x}^i$ as a parametrization of the interface Γ^i, with $\mathbf{n}^i$ being the outward pointing unit normal vector of Γ^i. Equation (22) is general in that it is true for curves and surfaces.

For the purpose of our time-discrete problem, we need to calculate $\kappa^{i+1}\mathbf{n}^i$ because it appears in the pressure boundary condition. This is accomplished by defining an appropriate approximation[83] and using (21):

$$\begin{aligned}
\kappa^{i+1}\mathbf{n}^i &= -\Delta_{\Gamma^i}\mathbf{x}^{i+1}, \\
&= -\Delta_{\Gamma^i}(\mathbf{x}^i + \delta t_{i+1}\mathbf{u}^{i+1}), \\
&= \kappa^i\mathbf{n}^i - \delta t_{i+1}\Delta_{\Gamma^i}\mathbf{u}^{i+1},
\end{aligned} \tag{23}$$

which is semi-implicit because everything is computed on the current boundary Γ^i.

C. Variational Form

We proceed to derive a variational formulation of the PDE by the standard means[72,80], as that will facilitate the use of a finite element method. Let $\mathbf{v}$ be an arbitrary smooth vector field test function for the velocity $\mathbf{u}$. Multiply the first equation in (20) by $\mathbf{v}$ and integrate:

$$\frac{\alpha}{\delta t_{i+1}}\int_{\Omega^i}(\mathbf{u}^{i+1}-\mathbf{u}^i)\cdot\mathbf{v} + \beta\int_{\Omega^i}\mathbf{u}^{i+1}\cdot\mathbf{v} + \int_{\Omega^i}\nabla p^{i+1}\cdot\mathbf{v} = 0. \tag{24}$$

Next, integrate the pressure gradient term by parts, plug in the boundary condition in (20), and rearrange to get

$$\begin{aligned}
&\left(\frac{\alpha}{\delta t_{i+1}} + \beta\right)\int_{\Omega^i}\mathbf{u}^{i+1}\cdot\mathbf{v} \\
&\quad - \int_{\Omega^i}p^{i+1}\nabla\cdot\mathbf{v} + \int_{\Gamma^i}\lambda^{i+1}\mathbf{n}^i\cdot\mathbf{v} \\
&\quad + D_{\text{visc}}\int_{\Gamma^i}(\mathbf{u}^{i+1}\cdot\mathbf{n}^i)(\mathbf{v}\cdot\mathbf{n}^i) \\
&\quad + \int_{\Gamma^i}\kappa^{i+1}\mathbf{n}^i\cdot\mathbf{v} \\
&= \frac{\alpha}{\delta t_{i+1}}\int_{\Omega^i}\mathbf{u}^i\cdot\mathbf{v} - \int_{\Gamma^i}E^i\mathbf{v}\cdot\mathbf{n}^i.
\end{aligned} \tag{25}$$

The semi-implicit curvature is rewritten by using (23)

$$\begin{aligned}
\int_{\Gamma^i}\kappa^{i+1}\mathbf{n}^i\cdot\mathbf{v} &= -\int_{\Gamma^i}\Delta_{\Gamma^i}(\mathbf{x}^i + \delta t_{i+1}\mathbf{u}^{u+1})\cdot\mathbf{v}, \\
&= \int_{\Gamma^i}\nabla_{\Gamma^i}(\mathbf{x}^i + \delta t_{i+1}\mathbf{u}^{u+1})\cdot\nabla_{\Gamma^i}\mathbf{v},
\end{aligned} \tag{26}$$

and integration by parts on Γ^i of $\Delta_{\Gamma^i} = \nabla_{\Gamma^i}\cdot\nabla_{\Gamma^i}$. Hence, the momentum equation becomes

$$\begin{aligned}
&\left(\frac{\alpha}{\delta t_{i+1}} + \beta\right)\int_{\Omega^i}\mathbf{u}^{i+1}\cdot\mathbf{v} \\
&\quad - \int_{\Omega^i}p^{i+1}\nabla\cdot\mathbf{v} + \int_{\Gamma^i}\lambda^{i+1}\mathbf{v}\cdot\mathbf{n}^i \\
&\quad + D_{\text{visc}}\int_{\Gamma^i}(\mathbf{u}^{i+1}\cdot\mathbf{n}^i)(\mathbf{v}\cdot\mathbf{n}^i) \\
&\quad + \delta t_{i+1}\int_{\Gamma^i}\nabla_{\Gamma^i}\mathbf{u}^{u+1}\cdot\nabla_{\Gamma^i}\mathbf{v} \\
&= \frac{\alpha}{\delta t_{i+1}}\int_{\Omega^i}\mathbf{u}^i\cdot\mathbf{v} \\
&\quad - \int_{\Gamma^i}E^i\mathbf{v}\cdot\mathbf{n}^i - \int_{\Gamma^i}\nabla_{\Gamma^i}\mathbf{x}^i\cdot\nabla_{\Gamma^i}\mathbf{v}.
\end{aligned} \tag{27}$$

The variational form of the second (conservation of mass) equation in (20) is obtained simply by multiplying by an arbitrary smooth test function q and integrating:

$$\int_{\Omega^i}q\nabla\cdot\mathbf{u}^{i+1} = 0. \tag{28}$$

In the following sections, we define $\mathbf{u}^{\text{old}} := \mathbf{u}^i$ and we drop the time-index i notation to simplify the presentation.

D. Variational Inequality for Pinning

The variational formulation provides a natural way to include the contact line pinning model. This is a crucial instance where the variational technique is able to improve on our previous level set method[21]. It is not known, to the best of our knowledge, how to implement the discontinuous switch (see Figure 7) in a stable and accurate way within the level set method.

In our framework, we treat λ as an extra unknown that must be solved for and acts as an inequality constraint on the velocity $\mathbf{u}$. Hence, an additional equation to (27) and (28) is required to close the system. Therefore, we append a variational inequality to our previous variational form[74,88,89]. The derivation is as follows.

First, let Λ be the set of functions on Γ defined by

$$\Lambda = \{\mu : |\mu| \leq P_{\text{pin}}\}, \tag{29}$$

which is a convex set. Physically, it is the set of (non-dimensional) pressure functions on the interface with absolute value limited to P_{pin}. Assume that the pinning relation is true (i.e. $\lambda = P_{\text{pin}}\text{sgn}(\mathbf{u}\cdot\mathbf{n})$). Then the following inequality

$$(\mathbf{u}\cdot\mathbf{n})\mu \leq (\mathbf{u}\cdot\mathbf{n})\lambda \tag{30}$$

is true for all μ in Λ for the following reason. If $\mathbf{u}\cdot\mathbf{n} = 0$, (30) is clearly satisfied. If $\mathbf{u}\cdot\mathbf{n} > 0$, then $\lambda = P_{\text{pin}}$ so

$$\mu \leq \lambda, \tag{31}$$

because μ is in Λ. Multiplying (31) by $\mathbf{u} \cdot \mathbf{n} > 0$ gives (30). If $\mathbf{u} \cdot \mathbf{n} < 0$, then $\lambda = -P_{\text{pin}}$ thus

$$\mu \geq \lambda, \tag{32}$$

because μ is in Λ. Multiplying (32) by $\mathbf{u} \cdot \mathbf{n} < 0$ gives (30). Equation (30) is called a *complementarity* condition between the normal velocity and the pinning variable. Upon rearranging (30) and integrating, we get

$$\int_\Gamma (\mathbf{u} \cdot \mathbf{n})(\mu - \lambda) \leq 0, \text{ for all } \mu \text{ in } \Lambda, \tag{33}$$

which is the *variational inequality* we need to complete our formulation. The preceding argument shows that assuming the pinning model $\lambda = P_{\text{pin}}\text{sgn}(\mathbf{u} \cdot \mathbf{n})$ implies equation (33). It is also true that (33) implies the pinning model[74,88], so they are equivalent. We omit the details.

The variational inequality allows us to treat λ as an additional unknown, and embeds the relation (18) into the act of solving the weak formulation. This is advantageous because it avoids introducing a discontinuous function into our method and it captures the inequality constraint exactly.

E. Variational Equations

For convenience, we introduce the following notation. We define the bilinear and linear forms:

$$a(\mathbf{u}, \mathbf{v}) = \left(\frac{\alpha}{\delta t} + \beta\right) \int_\Omega \mathbf{u} \cdot \mathbf{v} \\ + \delta t \int_\Gamma \nabla_\Gamma \mathbf{u} \cdot \nabla_\Gamma \mathbf{v} + D_{\text{visc}} \int_\Gamma (\mathbf{u} \cdot \mathbf{n})(\mathbf{v} \cdot \mathbf{n}), \tag{34}$$

$$b(\mathbf{v}, q) = -\int_\Omega q \nabla \cdot \mathbf{v}, \tag{35}$$

$$\chi(\mathbf{v}) = \frac{\alpha}{\delta t} \int_\Omega \mathbf{u}^{\text{old}} \cdot \mathbf{v} - \int_\Gamma E\mathbf{v} \cdot \mathbf{n} - \int_\Gamma \nabla_\Gamma \mathbf{x} \cdot \nabla_\Gamma \mathbf{v}. \tag{36}$$

With (34), (35), and (36), we can rewrite the variational form more concisely: find a solution $(\mathbf{u}, p, \lambda)$ such that

$$a(\mathbf{u}, \mathbf{v}) + b(\mathbf{v}, p) + \int_\Gamma \lambda(\mathbf{v} \cdot \mathbf{n}) = \chi(\mathbf{v}), \\ b(\mathbf{u}, q) = 0, \tag{37} \\ \int_\Gamma (\mathbf{u} \cdot \mathbf{n})(\mu - \lambda) \leq 0,$$

for all smooth test functions $\mathbf{v}$ and q defined on Ω and all μ in Λ. This is called a mixed variational formulation and falls into the framework of[78,90]. Thus, our algorithm consists of solving (37) to obtain the velocity, at each time-step t_i, followed by using the update equation (21) to move the droplet domain Ω. The proper function spaces to use in (37) and its well-posedness are discussed in[25] and a future publication.

F. Finite Element Method

1. Solving the Variational Equations

The variational setting that we have transformed our model into naturally facilitates the use of finite elements[79,80,90]. In solving (37), we use a finite element discretization. This involves expanding the solution variables $(\mathbf{u}, p, \lambda)$ and the test functions $(\mathbf{v}, q, \mu)$ using a finite-dimensional set of basis functions. This translates (37) into a finite dimensional linear system that must be solved at each time-step. In our case, there is an inequality constraint on part of the solution vector due to the third equation in (37). This requires the use of an iterative method to solve the system in order to compute the pinning model correctly[25].

The finite-dimensional basis functions are obtained by first partitioning the domain Ω (and Γ) into a set of triangles (and sides). On each triangle, we represent the velocity $\mathbf{u}$ with quadratic polynomials for each component, and a linear polynomial for the pressure p; the piecewise polynomials for $\mathbf{u}$ and p are globally continuous (Taylor-Hood elements[78,90]). On each side of the polygonal boundary, λ is represented by a constant value. In addition, we use piecewise quadratic curves to represent the interface Γ (i.e. the triangles on Γ have a curved side on Γ). For the 'curved' triangles, iso-parametric elements are used[79,80,90]; this is done to ensure accurate computation of surface tension forces (i.e. the curvature)[25].

2. Updating the Interface

Updating the domain mesh can be done using $\mathbf{u}$ and equation (21) evaluated at the mesh node positions. However, if the droplet develops a thin neck region, then the gradient of velocity can be quite large across the neck. Updating the mesh with this velocity would lead to severe mesh distortion. A simple remedy for this is to use a smooth extension of $\mathbf{u}\big|_\Gamma$ to a new vector function $\mathbf{u}_{\text{ext}}$ defined on all of Ω for updating the domain. This can be done by letting $\mathbf{u}_{\text{ext}}$ solve the following vector Laplace equation (harmonic extension)[26]:

$$-\nabla^2 \mathbf{u}_{\text{ext}} = 0, \text{ in } \Omega, \\ \mathbf{u}_{\text{ext}} = \mathbf{u}, \text{ on } \Gamma. \tag{38}$$

This guarantees that the shape of the domain will update the same (because $\mathbf{u}_{\text{ext}} = \mathbf{u}$ on Γ). It is a classical result that the solution of (38) minimizes $\int_\Omega |\nabla \mathbf{u}_{\text{ext}}|^2$[72], which is desirable because large gradients in the velocity cause mesh distortion[26]. This allows for smoothly updating the mesh node positions at each time step. Of course, in the case of large deformations even this method will fail, and a remedy for this is discussed in the next section.

3. Handling Large Deformations and Topological Changes

One of the drawbacks of using the front tracking method is the presence of the mesh. Because the interface is moving, the underlying mesh must move with it. If the droplet is undergoing a large deformation, such as a splitting motion, this can cause mesh distortion (i.e. elongated triangles in the droplet triangulation and/or inverted triangles). It is known that distorted meshes can adversely affect the accuracy of the finite element solution[79,91]. Therefore, any explicit front tracking method must also have a mechanism to correct severe mesh distortion.

We handle large mesh deformations by using harmonic extension (see the previous section), mesh smoothing, and periodic re-meshing. Allowing for topological changes requires a more advanced method. In this paper, we use a hybrid variational/level-set method developed in[26], which hinges on the fact that topological changes are rare events in time and local in space - we use the level-set method only when and where we need it. The hybrid method, to be reported in a future publication, exploits the best characteristics of both the level set and variational front tracking methods. We give some highlights of the algorithm in the following list. For more details, see[26].

- Mesh smoothing and re-meshing. We use standard techniques, such as optimization based mesh smoothing[92] and re-meshing with the program 'Triangle'[93].

- Updating mesh topology. We use the level set method during just one time step to guide the evolution of the explicit finite element mesh through a topological change.

- Mesh reconstruction after the topological change. We use an active contour-based minimization approach to adjust the mesh in the local region of the topological change and conform to the zero level contour of the level set function. This provides a new numerically-sound Lagrangian mesh for continuation of the variational front-tracking finite element method.

IV. RESULTS

We present direct visual comparisons and quantitative error measurements between our simulation method and five different experiments available from our collaborators at UCLA. In each section, we describe the experimental setup and the corresponding simulation results. The inclusion of contact line pinning and de-pinning in our model is required to predict the experimentally observed fluid shapes. Without it, the simulated fluid would always return to perfectly circular shapes under the action of surface tension, something that does not happen in experiments (see especially Figure 14). Simulations

for all experiments were run using the parameters listed in Table III.

A physical parameter D_{visc} was fit to the cases that we compare to. Accurate data for D_{visc} for realistic substrates/liquids is not easily available thus we experimented with different values for D_{visc}. For example, the splitting water droplet experiment in Section IV C splits at time $t = 131.4$ ms for $D_{\mathrm{visc}} = 0.359$ N s / m^2 (see Table III). Increasing D_{visc} by 20% increases the time to split by 16.8%. Decreasing D_{visc} by 20% decreases the time to split by 16.7%. This suggests a reasonable sensitivity for this parameter. We note that the general shape evolution looks visually the same (disregarding the time-scale) when varying D_{visc}.

We illustrate where the interface is pinned and not pinned in the visual comparisons by evaluating the behavior of λ and plotting the pinned portion of that boundary in gray. If $|\lambda| < P_{\mathrm{pin}}$ on some region of the interface, then we say that region is pinned since this guarantees that $\mathbf{u} \cdot \mathbf{n} = 0$ (recall Section III D). However, if $|\lambda| = P_{\mathrm{pin}}$, this does *not* imply that $\mathbf{u} \cdot \mathbf{n} \neq 0$. It is still possible that $\mathbf{u} \cdot \mathbf{n} = 0$ which is consistent with our formulation. In other words, a droplet could have zero velocity everywhere but certain portions of the boundary may barely overcome the pinning force yet not have enough force left to move.

For experiments exhibiting topological changes, a numerical tolerance was used in allowing pinch-off of thin neck regions. Since the assumed vertically-averaged Hele-Shaw model is meaningless for horizontal length scales much smaller than the channel height H, setting this pinch-off tolerance to $H/2$ is reasonable (recall that the device height H is approximately 20 times smaller than the electrode pitch and typical droplet size).

The error between the experiment and simulation, at each time, is defined as the area of the liquid domain mismatch (left panel in Figure 8) divided by the sum of the areas of the experimental and simulated domains (center and right panels in Figure 8)

$$\mathrm{Error}(t) = \frac{|\Omega_{\mathrm{exp}}(t) \cup \Omega_{\mathrm{sim}}(t) - \Omega_{\mathrm{exp}}(t) \cap \Omega_{\mathrm{sim}}(t)|}{|\Omega_{\mathrm{exp}}(t)| + |\Omega_{\mathrm{sim}}(t)|}. \tag{39}$$

Here Ω_{exp} and Ω_{sim} denote the measured and simulated liquid regions, $|\cdot|$ denotes the area of each region, and $\cup$, $\cap$, and $-$ denote set union, intersection, and difference (respectively). If the experiment and simulation match perfectly, then Error = 0; if they are completely disjoint, Error = 1. We computed (39) via image processing tools contained in MATLAB, in addition to using a level set active contour algorithm[94] to extract a closed polygon representing the experimental droplet's boundary. With this definition, the quantitative error between the experiment and our simulation, for all the experiments, is shown in Figure 9.

The order of cases is organized from the easiest to the most difficult to model. We start with motion of just one droplet on a simple and then a more complex path (Sections IV A and IV B); then we consider splitting of a single droplet, of water and then glycerin (Sections IV C
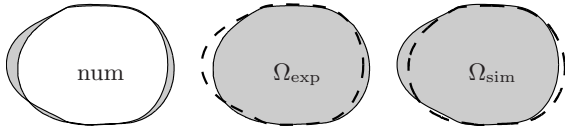
FIG. 8: Visual description of our error metric (39). Experimental and simulated droplet boundaries are taken from the last frame of Figure 10 and are re-plotted 3 times above for clarity. The shaded region in the left panel corresponds to the numerator of (39), i.e. the set of points denoted by $\Omega_{\mathrm{exp}} \cup \Omega_{\mathrm{sim}} - \Omega_{\mathrm{exp}} \cap \Omega_{\mathrm{sim}}$. The center panel highlights the experimental droplet (shaded region). The right panel highlights the simulated droplet.

and IV D); and we end with the joining of two water droplets that leads to a final combined droplet that remains pinned in a significantly non-circular shape (Section IV E), a shape that could not be modeled without the inclusion of pinning.

A. Moving Glycerin Droplet

The EWOD device in this experiment has only two electrodes arranged in a horizontal fashion with a droplet of glycerin being actuated. A voltage of 50 volts is first applied to the left electrode with 0 volts on the right. This causes the droplet to flow to the left electrode. The voltage actuation is kept constant for two seconds when it switches to 0 volts on the left, 50 volts on the right, which causes the droplet to switch direction of motion. Again, the voltage actuation is kept constant until after two seconds it switches back, causing the droplet to also switch its direction of travel. This process repeats.

Figure 10 shows a comparison between the simulation and the experiment. There is some uncertainty in the physical parameters of the fluid in this case. Glycerin is highly hygroscopic[95] and, in particular, its viscosity varies significantly with only a small volume fraction of water[95]; viscosity values vary by a factor of 20 for water percentages of 0% to 20%. Moreover, temperature also has a large effect; a 10 degree Celsius change (for low water volume fraction) can affect its viscosity by a factor of 2. The experiments were not performed in a humidity controlled environment, thus there is some uncertainty in the actual viscosity of the fluid. After discussing the details of the experiments with our UCLA collaborators, we found it reasonable to assume a water percentage between 20% and 10% at 20 degrees Celsius. Because there is no way of ascertaining the exact composition of the fluid, we had no other choice.

The pinning coefficient $c_{\mathrm{pin}} = 3.0$ mN / m was taken to be the same as for water. We do not have data for the pinning coefficient of glycerin, but we do have data for water (from our past inclined plane experiments which were conducted with a range of liquids that included water but not glycerin). The drag coefficient $D_{\mathrm{visc}} = 5.0$ N s / m² was fit to ensure that the simulated droplet moved with the same speed as in the experiment. The

value of D_{visc} is much higher than for water (see Sections IV B and IV C). This is reasonable given the higher viscosity of glycerin. Also recall that viscosity affects the time-scale of motion, which varies considerably with water volume fraction. In this case, we assumed a 90%/10% glycerin/water mixture. Assuming a higher water percentage produces significantly higher values for D_{visc}, but this does not significantly affect the shape evolution of the droplet.

B. Moving Water Droplet

The EWOD device shown in this example has eight electrodes arranged in a square-like pattern. A predetermined voltage sequence was used to actuate the droplet. The time-varying voltages act to modulate the pressure boundary conditions such that the droplet moves to the right first, then up, to the left, and finally downwards. In our simulation, the value of D_{visc} was *not* fit to this experiment. Instead, we set the viscous damping to be the same as for the case in Section IV C ($D_{\mathrm{visc}} = 0.359$ N s/m², see Table III). Thus, the physical parameters for this case and in Section IV C are exactly the same. Note that the physical constants for water are very stable across a wide range of experimental conditions.

Figure 11 shows the moving droplet experiment with our simulation results overlaid. It is evident that the simulation follows the experiment fairly well; the overall motion and time scale are correct. The match is not exact, however, and this is because of parametric uncertainty and because our contact line pinning model only approximates the true physics.

C. Splitting Water Droplet

In Figure 12, an overhead view of an EWOD device with three electrodes running left to right is depicted with a splitting droplet. The construction of this device is exactly the same as in Section IV B, except the electrode grid pattern is different. The voltage actuation, from left to right, is 25 volts, 0 volts, 25 volts and is constant throughout the split. In the first frame, an initial near-circular droplet is shown just before voltage activation. After the voltage is turned on, the liquid-gas interface over the left and right electrodes deforms and induces a low pressure region there. The regions where no voltage is activated remain at high pressure. In the subsequent frames, the droplet is pulled from the left and right sides, while it is pushed in from the top and bottom. The droplet elongates along the horizontal dimension and is being pinched in the vertical direction. This causes two daughter droplets to form on the left and right sides, with a thin neck joining them. The neck eventually gets so thin that it snaps due to capillary instability. The two smaller droplets then continue moving to the left and right electrodes because of the pressure differential created from the voltage actuation. Finally, the

TABLE III: Simulation parameters for all experiments in Section IV. Note the large viscosity of glycerin, which varies significantly with the volume fraction of water. $\theta_{b,0V}$, $\theta_{b,50V}$, $\theta_{b,65V}$ are the contact angles on the bottom plate of the EWOD device at 0, 50, and 65 volts, respectively. Each simulation uses a different value of U_0 so the maximum non-dimensional velocity is close to unity. This also causes Re, Ca, α, β, and t_0 to differ.

	Moving Glycerin[a]	Moving Water[b]	Splitting Water[c]	Splitting Glycerin[d]	Joining Water[e]	Units
σ_{lg}	0.06422	0.07199	0.07199	0.0657	0.07199	J / m^2
μ	384.467	0.89	0.89	59.9	0.89	g / m s
ρ	1240.40	996.93	996.93	1208.5	996.93	kg / m^3
H	0.1	0.07	0.07	0.1	0.1	mm
L_{Elec}	1.5	1.4	1.4	1.5	1.5	mm
L	3.0	4.2	4.2	4.5	4.5	mm
U_0	0.8	50	20	2	15	mm / sec
t_0	3750	84	210	2250	300	ms
P_0	21.41	17.14	17.14	14.6	15.998	N / m^2
c_{pin}	0.003	0.003	0.003	0.003	0.003	J / m^2
D_{visc}	5.000	0.359	0.359	5.100	1.995	N s / m^2
Re	2.5810E-4	3.92	1.57	4.0351E-3	1.6802	non-dim.
Ca	4.7894E-3	6.1814E-4	2.4726E-4	1.8234E-3	1.8544E-4	non-dim.
α	3.7085E-5	0.145406	2.3265E-2	3.3110E-4	1.4021E-2	non-dim.
β	51.725	26.7037	10.6815	44.310	4.5063	non-dim.
$\theta_{b,0V}$	107.35	-	-	107.35	111.62	degrees
$\theta_{b,50V}$	68.46	-	-	-	-	degrees
$\theta_{b,65V}$	-	-	-	64.32	70.01	degrees

[a]Section IV A, 90%/10% glycerin/water mixture.
[b]Section IV B.
[c]Section IV C.
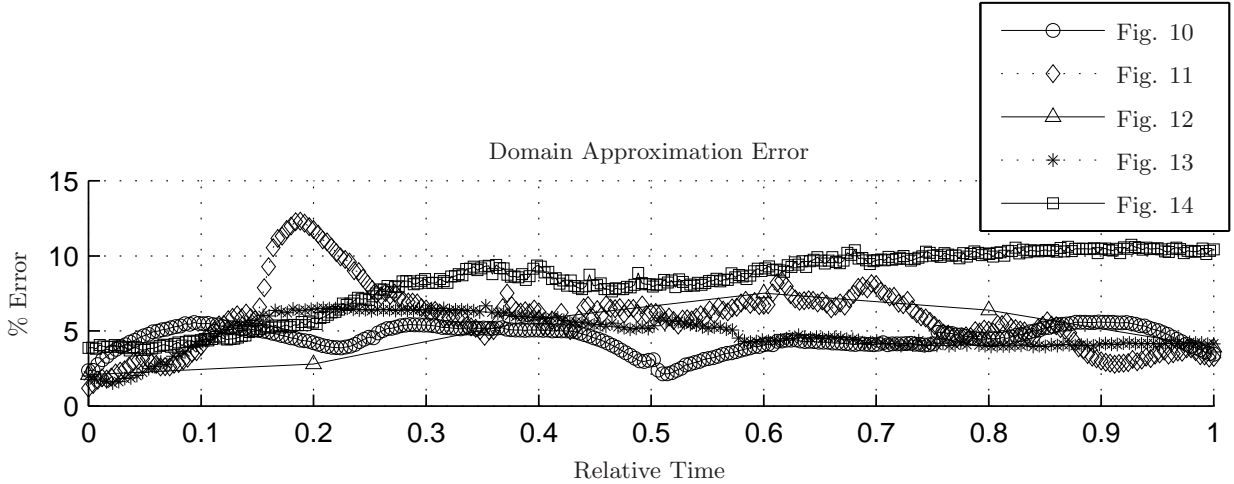[d]Section IV D 80%/20% glycerin/water mixture.
[e]Section IV E.

FIG. 9: Error between experimental droplet shape and simulated shape versus normalized time for all experiments. The error was measured using equation (39). Not all experiments have the same number of video frames (i.e. the experiment corresponding to Figure 12 has only 6 video frames for the whole experiment). The overall error is reasonable. We also measured the frame-to-frame error for all experiments except Figure 12. The frame-to-frame error is defined as the difference, via (39), between the extracted polygonal representation of the experimental drop in consecutive video frames. The average frame-to-frame error (over each experiment) for extracting a polygonal representation of the experimental droplet boundary is less than 0.7%. The maximum frame-to-frame error is less than 2%.

two droplets come to rest on the two 25 volt electrodes. The total time of this experiment is approximately 167 milliseconds.

The contact line pinning coefficient is taken from our past, independent inclined-plane experiments and was found to be $c_{\mathrm{pin}} = 3$ mN / m. The interface drag constant is chosen to make the simulation time-scale match the experiment: $D_{\mathrm{visc}} = 0.359$ N s/m^2. See Figure 12 for an overlay of the variational simulation with the experiment. The value of D_{visc} is reasonable and is comparable
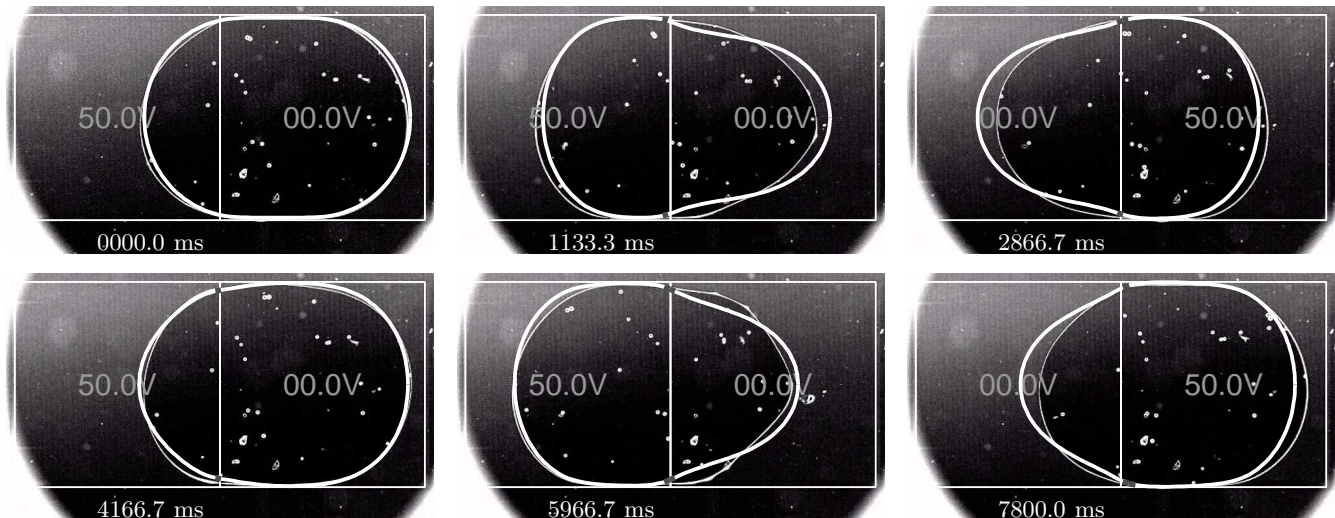
FIG. 10: Moving glycerin droplet experimental results with simulation overlay. The solid curve represents the simulated droplet boundary with small grayed regions (near the electrode edge) denoting pinned portions of the boundary. Frames show video snapshots of the experiment (courtesy of CJ Kim and Jian Gong at UCLA). The applied voltage (50 volts) switches between the left and right electrodes every two seconds. Each electrode is square with a side length of 1.5 mm. Simulation and device parameters are given in Table III. Note the large time-scale because glycerin is highly viscous. The simulation follows the experiment fairly well, except there is some lagging in the 'tail' region (enhanced online).

to the values listed in[96] for a column of fluid comprised of deionized water between two parylene coated electrodes.

D. Splitting Glycerin Droplet

The EWOD device in this experiment has three electrodes arranged in a horizontal fashion with a glycerin droplet being actuated to split apart. The device construction is not the same as in the previous cases (see Table III). A voltage of 65 volts is applied to the left and right electrodes, with 0 volts applied on the center electrode which causes the droplet to pull apart. The voltage actuation is constant throughout the experiment. Eventually, a thin neck develops between two smaller droplets and the neck pinches.

Figure 13 shows a comparison between the simulation and the experiment. Just as in Section IV A, there is some uncertainty in the physical parameters of the fluid. Here, we assume an 80%/20% glycerin/water mixture with similar values for the pinning coefficient and viscous damping as in Section IV A ($c_{\mathrm{pin}} = 3$ mN / m and $D_{\mathrm{visc}} = 5.1$ N s/m^2). The value of c_{pin} was taken to be the same as for water and D_{visc} was fit to match the time-scale of this experiment. If we assumed the same glycerin/water mixture as in Section IV A (i.e. 90%/10%), then even with setting $c_{\mathrm{pin}} = 0$ and $D_{\mathrm{visc}} = 0$ the simulated droplet moved significantly slower than the experiment. In other words, the viscosity was over estimated. Therefore, we thought it reasonable to assume a higher water percentage in this case (lower effective viscosity). This experiment was not run simultaneously with the experiment in Section IV A, so there is no reason to assume

the fluid parameters to be the same.

E. Joining Water Droplets

This experiment uses the same EWOD device as in Section IV D, except that two droplets of water are being actuated to join together. A voltage of 65 volts is applied to the center electrode, with 0 volts applied to the left and right electrodes, which causes the two droplets to flow together. The voltage actuation is constant throughout the experiment. Eventually, the two droplets connect and merge together. Figure 14 shows a comparison between our simulation and the experiment. The grayed regions of the solid curve in the figure represent pinned portions of the boundary (i.e. these regions of the interface do not move in the normal direction). In the last frame, the droplet has essentially come to rest. The lack of pinned regions is because the droplet is asymptotically approaching a pinned state. Running the simulation to a time level of $t = 2.8$ s shows a more completely pinned droplet. However, the experimental recording was terminated much earlier. The difference between the simulated droplet in the last frame of Figure 14 and the pinned state at $t = 2.8$ s is on the order of micro-meters.

V. CONCLUSION

We have presented a model of fluid droplet motion in planar electrowetting on dielectric (EWOD) devices. Our model is derived from first principles where possible, is based on independent experimental data where
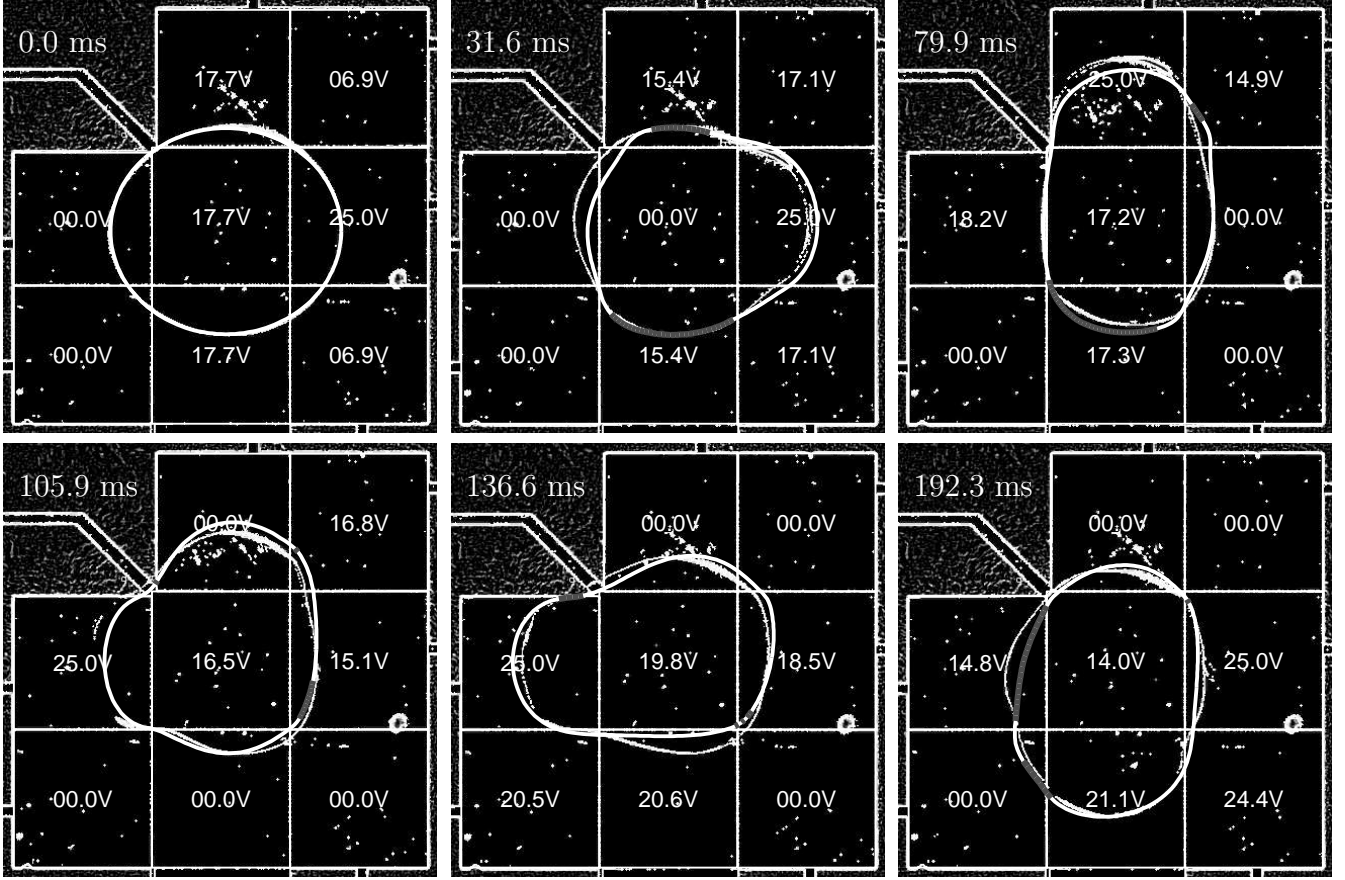
FIG. 11: Moving water droplet motion experimental results with simulation overlay (solid curve is the simulation). Six frames show video snapshots of the experiment (courtesy of CJ Kim and Jian Gong at UCLA). A time-varying sequence of voltages is applied to the eight electrode pattern so as to make the droplet move right, up, left, then down. Each electrode is square with a side length of 1.4 mm. All physical parameters here are the same as for the splitting experiment shown in Figure 12 except the electrode pattern is different. The gray regions of the simulated droplet boundary represent pinned portions of the liquid-gas interface, meaning they do not move in the normal direction. Note that we do not specify where the droplet is pinned; this is obtained from solving the variational inequality. As can be seen, the simulated droplet follows the real droplet fairly closely (enhanced online).

first-principle descriptions are not feasible, and it contains only one fitting parameter. The fluid dynamics is modeled by Hele-Shaw type equations with a focus on including the relevant boundary phenomena. Specifically, we have included a physically meaningful contact line force-threshold pinning model which was motivated by experimental observations in the literature. This description is sufficiently simple to be incorporated into device length and time scale simulations yet it enables much improved predictions of device behavior.

We have also presented a semi-implicit variational front-tracking method that is able to handle surface tension, conservation of mass, our non-linear contact line pinning description, and viscous interface damping in a straightforward manner. The model was discretized via the finite element method using MATLAB/C++ and yields simulations that evaluate between 5 and 15 minutes on a laptop and that compared very well to experiments. Specifically, we have compared our simulations to prior available experimental data for five different cases of

droplet motion that include splitting, joining, and partial pinning of droplets and have observed good agreement. Our model is fast but accurate. To our best knowledge, it is the only model currently available that can simulate total system dynamics, on device length and time scales, but includes key loss effects due to both contact angle saturation and line pinning. The model better predicts experimentally observed electrowetting behavior and is appropriate for system design, optimization, and control.
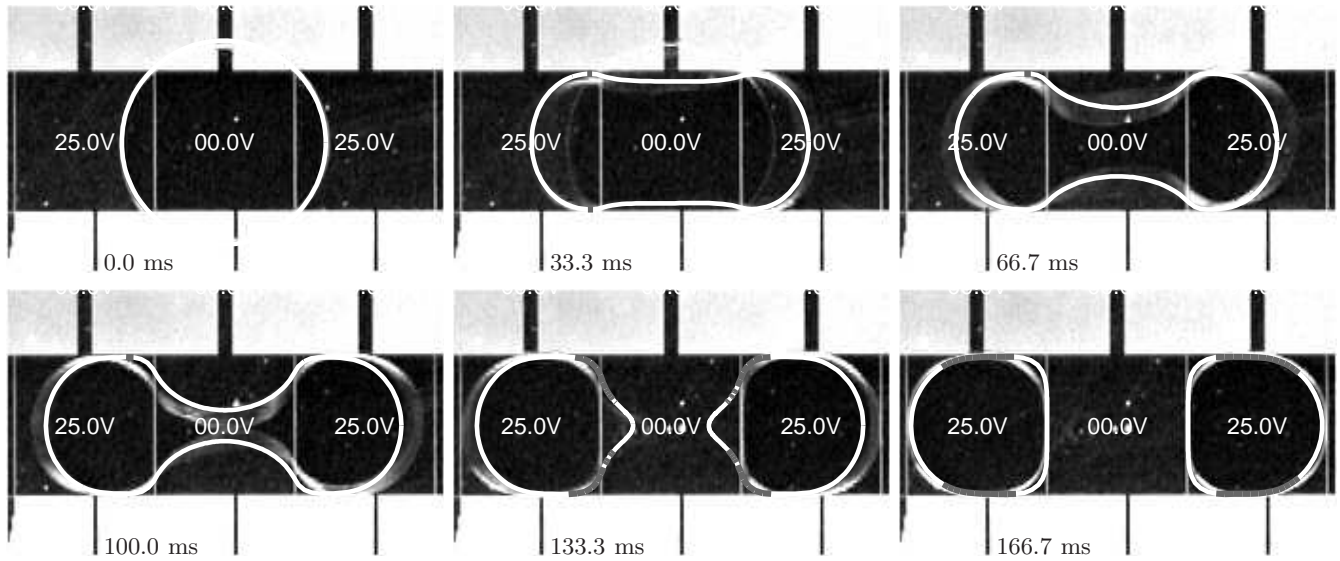
FIG. 12: Splitting water droplet experimental results with simulation overlay (solid curve is the simulation). Six frames show video snapshots of the experiment (courtesy of CJ Kim and Sung Kwon Cho at UCLA). The three electrodes shown in each frame have activation voltages (from left to right) of 25, 0, and 25 volts. Each electrode is approximately square with a side length of 1.4 mm. The gray regions of the simulated boundary indicate where the interface is pinned (i.e. cannot move in the normal direction). Only one parameter D_{visc} was fit to the simulation in order to match the time-scale of the experiment.
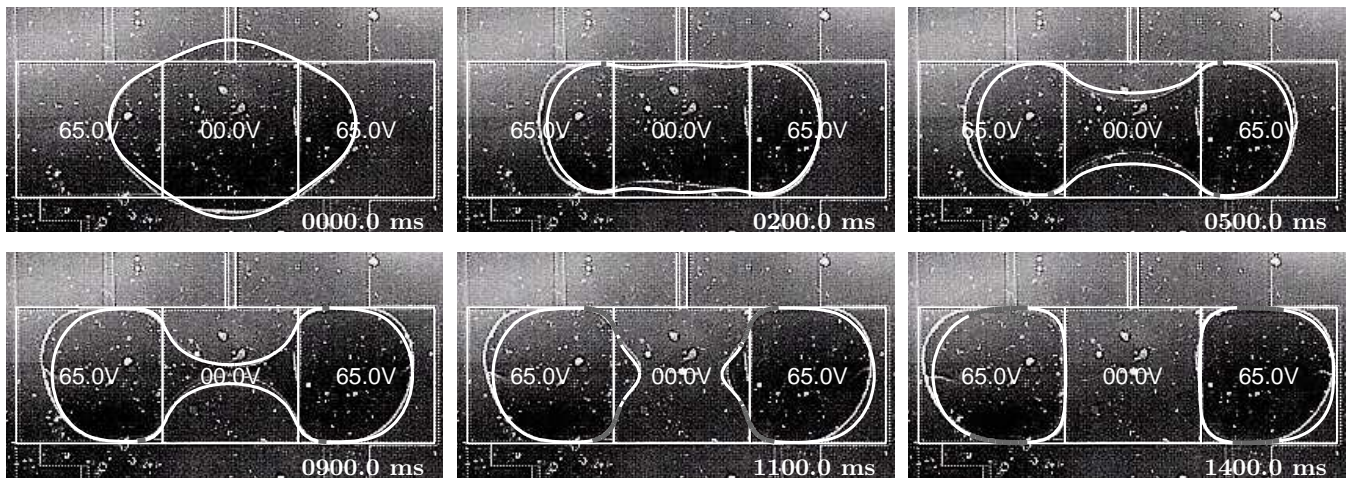

FIG. 13: Splitting Glycerin droplet experimental results with simulation overlay (solid curve is the simulation). Frames show video snapshots of the experiment (courtesy of CJ Kim and Jian Gong at UCLA). The applied voltage (65 volts on the left and right electrodes) causes the droplet to be pulled apart and eventually split. Each electrode is approximately square with a side length of 1.5 mm. The match between the simulation and experiment is very good. In particular, note the relaxation of the interface immediately after pinch-off ($t = 1100$ milliseconds). The only difference is that, in the experiment, slightly more fluid flows into the left satellite droplet than into the right droplet (as compared to the simulation). Also note the grayed regions of the boundary indicating pinned portions of the interface (enhanced online).

* Electronic address: walker@cims.nyu.edu   † Electronic address: benshap@eng.umd.edu
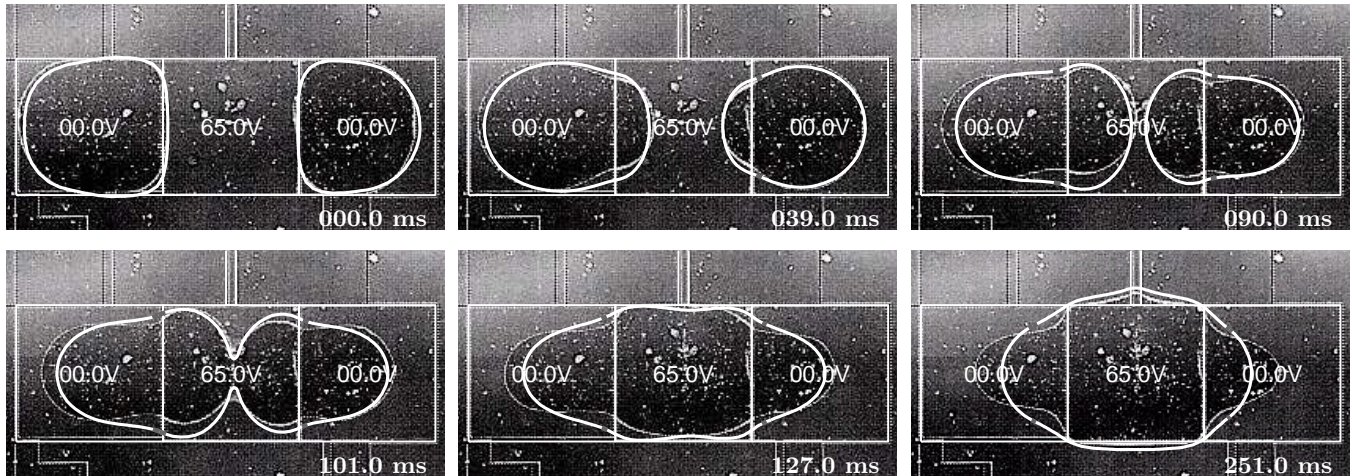
FIG. 14: Joining water droplets experimental results with simulation overlay (solid curve is the simulation). Frames show video snapshots of the experiment (courtesy of CJ Kim and Jian Gong at UCLA). The applied voltage (65 volts on the center electrode only) causes the two side droplets to flow together and eventually merge. Each electrode is approximately square with a side length of 1.5 mm. The simulation matches the experiment fairly well in the first four frames. However, the pinning behavior in the experiment is significantly different than the simulation in the last two frames. We believe that the sharp snap-together of the droplets during coalescence makes this case more sensitive to modeling uncertainties than the move or split cases (enhanced online).

[‡] Electronic address: rhn@math.umd.edu

[1] B. Berge and J. Peseux. Variable focal lens controlled by an external voltage: An application of electrowetting. *European Physical Journal E*, 3(2):159–163, 2000.

[2] Sung Kwon Cho, Hyejin Moon, and Chang-Jin Kim. Creating, transporting, cutting, and merging liquid droplets by electrowetting-based actuation for digital microfluidic circuits. *Journal of Microelectromechanical Systems*, 12 (1):70–80, 2003.

[3] Robert A. Hayes and B. J. Feenstra. Video-speed electronic paper based on electrowetting. *Nature*, 425(6956):383–385, 2003.

[4] Junghoon Lee, Hyejin Moon, Jesse Fowler, Thomas Schoellhammer, and Chang-Jin Kim. Electrowetting and electrowetting-on-dielectric for microscale liquid handling. In *Sensors and Actuators, A-Physics (95)*, page 269, 2002.

[5] F. Mugele and J.-C. Baret. Electrowetting: from basics to applications. *Journal of Physics: Condensed Matter*, 17: R705–R774, 2005.

[6] M.G. Pollack, R.B. Fair, and A.D. Shenderov. Electrowetting-based actuation of liquid droplets for microfluidic applications. *Applied Physics Letters*, 77(11), 2000.

[7] C. Quilliet and B. Berge. Electrowetting: a recent outbreak. *Current Opinion in Colloid & Interface Science*, 6 (1):34–39, 2001.

[8] H. Ren, R. B. Fair, M. G. Pollack, and E. J. Shaughnessy. Dynamics of electro-wetting droplet transport. *Sensors and Actuators B-Chemical*, 87(1):201–206, 2002.

[9] Thibault Roques-Carmes, Robert A. Hayes, B. J. Feenstra, and L. J. M. Schlangen. Liquid behavior inside a reflective display pixel based on electrowetting. *Journal of Applied Physics*, 95(8):4389–4396, 2004.

[10] Thibault Roques-Carmes, Robert A. Hayes, and L. J. M. Schlangen. A physical model describing the electro-optic behavior of switchable optical elements based on electrowetting. *Journal of Applied Physics*, 96(11):6267–6271, 2004.

[11] F. Saeki, J. Baum, H. Moon, J.-Y. Yoon, C.-J. Kim, and R. L. Garrell. Electrowetting on dielectrics (ewod): Reducing voltage requirements for microfluidics. *Polym. Mater. Sci. Eng.*, 85:12–13, 2001.

[12] E. Seyrat and R. A. Hayes. Amorphous fluoropolymers as insulators for reversible low-voltage electrowetting. *Journal of Applied Physics*, 90, 2001.

[13] H. J. J. Verheijen and W. J. Prins. Reversible electrowetting and trapping of charge: Model and experiments. *Langmuir*, 15:6616–6620, 1999.

[14] Christopher G. Cooney, Chao-Yi Chen, Michael R. Emerling, Ali Nadim, and James D. Sterling. Electrowetting droplet microfluidics on a single planar surface. *Microfluidics and Nanofluidics*, 2(5):435–446, 2006.

[15] N. Kumari, V. Bahadur, and S. V. Garimella. Electrical actuation of electrically conducting and insulating droplets using ac and dc voltages. *Journal of Micromechanics and Microengineering*, 18(10):105015, 2008.

[16] B. Berge. Électrocapillarité et mouillage de films isolants par l'eau (including an english translation). *Comptes Rendus de l'Académie des Sciences de Paris, Série II*, 317: 157–163, 1993.

[17] Benjamin Shapiro, Hyejin Moon, Robin Garrell, and Chang-Jin Kim. Equilibrium behavior of sessile drops under surface tension, applied external fields, and material variations. *Journal of Applied Physics*, 93, 2003.

[18] Sung Kwon Cho, Hyejin Moon, Jesse Fowler, S.-K. Fan, and Chang-Jin Kim. Splitting a liquid droplet for electrowetting-based microfluidics. In *International Mechanical Engineering Congress and Exposition*, New York, NY, Nov 2001. ASME Press. ISBN: 0791819434.

[19] J. Gong, S. K. Fan, and C. J. Kim. Portable digital microfluidics platform with active but disposable lab-on-chip. In *17th IEEE International Conference on Micro Electro*

Mechanical Systems (MEMS), pages 355–358, Maastricht, The Netherlands, Jan 2004. IEEE Press. ISBN: 0-7803-8265-x.

[20] Shawn W. Walker and Benjamin Shapiro. A control method for steering individual particles inside liquid droplets actuated by electrowetting. *Lab on a Chip*, 5: 1404–1407, October 2005.

[21] Shawn W. Walker and Benjamin Shapiro. Modeling the fluid dynamics of electrowetting on dielectric (ewod). *Journal of Microelectromechanical Systems*, 15(4):986–1000, August 2006.

[22] Karl Johan Aström and Richard M. Murray. *Feedback Systems: An Introduction for Scientists and Engineers*. Princeton University Press, Princeton, New Jersey, 2008.

[23] Alberto Isidori. *Nonlinear Control Systems (Communications and Control Engineering)*. Springer, 1995.

[24] Benjamin Shapiro, Hyejin Moon, Robin Garrell, and C.-J. Kim. Modeling of electrowetted surface tension for addressable microfluidic systems: Dominant physical effects, material dependences, and limiting phenomena. In *The Sixteenth Annual International Conference on Micro Electro Mechanical Systems (MEMS)*, pages 201– 205, Kyoto, Japan, Jan 2003. IEEE Press. ISBN: 0-7803-7744-3.

[25] Shawn W. Walker. *Modeling, Simulating, and Controlling the Fluid Dynamics of Electro-Wetting On Dielectric*. PhD thesis, University of Maryland, College Park, August 2007.

[26] Shawn W. Walker. A hybrid variational-level set approach to handle topological changes. Master's thesis, University of Maryland at College Park, May 2007.

[27] G. Lippmann. Relations entre les phénomènes électriques et capillaires. *Ann. Chim. Phys.*, 5:494–549, 1875.

[28] Jr-Lung Lin, Gwo-Bin Lee, Yi-Hsien Chang, and Kang-Yi Lien. Model description of contact angles in electrowetting on dielectric layers. *Langmuir*, 22(1):484–489, 2006.

[29] M. Vallet, M. Vallade, and B. Berge. Limiting phenomena for the spreading of water on polymer films by electrowetting. *The European Physical Journal B*, 11:583–591, 1999.

[30] V. Peykov, A. Quinn, and J. Ralston. Electrowetting: a model for contact-angle saturation. *Colloid Polymer Science*, 278:789–793, 2000.

[31] T. B. Jones. On the relationship of dielectrophoresis and electrowetting. *Langmuir*, 18:4437–4443, 2002.

[32] T. D. Blake, A. Clarke, and E. H. Stattersfield. An investigation of electrostatic assist in dynamic wetting. *Langmuir*, 16(6):2928–2935, 2000.

[33] C. Decamps and J. De Coninck. Dynamics of spontaneous spreading under electrowetting conditions. *Langmuir*, 16 (26):10150–10153, 2000.

[34] H.-W. Lu, K. Glasner, A. L. Bertozzi, and Chang-Jin Kim. A diffuse interface model for electrowetting drops in a heleshaw cell. *Journal of Fluid Mechanics*, 590:411 – 435, 2007.

[35] Anthony Quinn, Rossen Sedev, and John Ralston. Contact angle saturation in electrowetting. *The Journal of Physical Chemistry B*, 109(13):6268–6275, 2005.

[36] A. G. Papathanasiou, A. T. Papaioannou, and A. G. Boudouvis. Illuminating the connection between contact angle saturation and dielectric breakdown in electrowetting through leakage current measurements. *Journal of Applied Physics*, 103(3):034901, 2008.

[37] J.-C. Baret, B. Cross, A. Kumar, F. Mugele, and M. Pluntke. Finite conductivity effects and apparent contact angle saturation in ac electrowetting. In Ren Overney Michael Urbakh John T. Fourkas, Pierre Levitz, editor, *Dynamics in Small Confining Systems VIII*, volume 899E, pages 69–76, Boston, MA, 2005. Materials Research Society Symposium Proceedings.

[38] R. S. Burdon. *Surface Tension and the Spreading of Liquids*. Cambridge University Press, Cambridge, Great Britain, 1949.

[39] Editors: J. Drelich, J. S. Laskowski, and K. L. Mittal. *Apparent and Microscopic Contact Angles*. VSP BV, Zeist, The Netherlands, 2000.

[40] P.-G. de Gennes, F. Brochard-Wyart, and D. Quéré. *Capillarity and Wetting Phenomena: Drops, Bubbles, Pearls, Waves*. Springer-Verlag, New York, NY, 2004.

[41] E. Wolfram and R. Faust. *Wetting, Spreading and Adhesion*, chapter Liquid Drops on a Tilted Plate, Contact Angle Hysteresis and the Young Contact Angle. Academic Press, Leicestershire, England, 1978.

[42] E. Schaffer and P. Z. Wong. Dynamics of contact line pinning in capillary rise and fall. *Physical Review Letters*, 80(14):3069–3072, 1998.

[43] E. B. Dussan. On the ability of drops or bubbles to stick to non-horizontal surfaces of solids. part 2. small drops or bubbles having contact angles of arbitrary size. *Journal of Fluid Mechanics*, 151:1–20, Feb. 1985.

[44] A. Henning, U. Staudinger, K.-J. Eichhorn, K. Sahre, M. Rogalli, A. W. Neumann, and K. Grundke. Contact angle hysteresis: study by dynamic cycling contact angle measurements and variable angle spectroscopic ellipsometry on polyimide. *Langmuir*, 20:6685–6691, 2004.

[45] Jean Berthier, Philippe Dubois, Philippe Clementz, Patricia Claustre, Christine Peponnet, and Yves Fouillet. Actuation potentials and capillary forces in electrowetting based microsystems. *Sensors and Actuators A: Physical*, 134(2): 471 – 479, 2007.

[46] F. Li and F. Mugele. How to make sticky surfaces slippery: Contact angle hysteresis in electrowetting with alternating voltage. *Applied Physics Letters*, 92(24):244108, 2008.

[47] Jason S. Kuo, Paolo Spicar-Mihalic, Indalesio Rodriguez, and Daniel T. Chiu. Electrowetting-induced droplet movement in an immiscible medium. *Langmuir*, 19(2):250255, 2003.

[48] P.-G. de Gennes. Wetting: Statics and dynamics. *Reviews of Modern Physics*, 57:827–863, July 1985.

[49] J. Lienemann, A. Greiner, and J. G. Korvink. Modeling, simulation, and optimization of electrowetting. *IEEE Transactions on Computer-Aided Design of Integrated Circuits and Systems*, 25(2):234–247, Feb. 2006.

[50] K. Brakke. The surface evolver. *Experimental Mathematics*, 1(2):141–165, 1992.

[51] Kamran Mohseni and Ali Dolatabadi. An electrowetting microvalve: Numerical simulation. *Ann NY Acad Sci*, 1077:415–425, 2006.

[52] C. Eck, M. Fontelos, G. Grün, F. Klingbeil, and O. Vantzos. On a phase-field model for electrowetting. *to appear, Interfaces and Free Boundaries*, 2009.

[53] Viatcheslav Berejnov and Robert E. Thorne. Effect of transient pinning on stability of drops sitting on an inclined plane. *Physical Review E*, 75, 2007.

[54] Mark O. Robbins and J. F. Joanny. Contact angle hysteresis on random surfaces. *Europhysics Letters*, 3(6):729–735, 1987.

[55] J. P. Stokes, M. J. Higgins, A. P. Kushnick, S. Bhattacharya, and Mark O. Robbins. Harmonic generation as a probe of dissipation at a moving contact line. *Physical Review Letters*, 65(15):1885–1888, 1990.

[56] J. F. Joanny and Mark O. Robbins. Motion of a contact line on a heterogeneous surface. *Journal of Chemical Physics*, 92:3206–3212, March 1990.

[57] Suman Kumar, Daniel H. Reich, and Mark O. Robbins. Critical dynamics of contact-line motion. *Physical Review E*, 52:5776–5779, December 1995.

[58] H. S. Hele-Shaw. The flow of water. *Nature (London)*, 58:34–36, 1898.

[59] G. K. Batchelor. *An Introduction to Fluid Dynamics*. Cambridge University Press, New York, NY, 1967.

[60] M. P. do Carmo. *Differential Geometry of Curves and Surfaces*. Prentice Hall, Upper Saddle River, New Jersey, 1976.

[61] R. F. Probstein. *Physicochemical Hydrodynamics: An Introduction*. John Wiley and Sons, Inc., New York, 2nd edition, 1994.

[62] Yulii D. Shikhmurzaev. *Capillary Flows with Forming Interfaces*. Chapman & Hall/CRC, 1st edition, 2007. 480 pp.

[63] Editors: G. Pétré and A. Sanfeld. *Lecture Notes in Physics: Capillarity Today*. Springer-Verlag, New York, NY, 1990.

[64] J. A. Marsh, S. Garoff, and E. B. Dussan. Dynamic contact angles and hydrodynamics near a moving contact line. *Physical Review Letters*, 70(18):2778–2781, 1993.

[65] Peter A. Thompson and Mark O. Robbins. Simulations of contact-line motion: Slip and the dynamic contact angle. *Physical Review Letters*, 63(7):766–769, Aug 1989.

[66] M. Haataja, J. A. Nieminen, and T. Ala-Nissila. Molecular ordering of precursor films during spreading of tiny liquid droplets. *Physical Review E*, 52(3):R2165–R2167, Sep 1995.

[67] G. He and N. G. Hadjiconstantinou. A molecular view of tanner's law: molecular dynamics simulations of droplet spreading. *Journal of Fluid Mechanics*, 497:123–132, 2003.

[68] V. M. Samsonov and A. S. Ratnikov. Comparative molecular dynamics study of simple and polymer nanodroplet spreading. In *Colloids and Surfaces A: Physicochemical and Engineering Aspects*, volume 298, pages 52 – 57, Loughborough, UK, April 2007. XVIIth European Chemistry at Interfaces Conference, Elsevier.

[69] Daniel Bonn, Jens Eggers, Joseph Indekeu, Jacques Meunier, and Etienne Rolley. Wetting and spreading. *Reviews of Modern Physics*, 81(2):739, 2009.

[70] Terence D. Blake. The physics of moving wetting lines. *Journal of Colloid and Interface Science*, 299:1–13, 2006.

[71] Tiezheng Qian, Xiao ping Wang, and Ping Sheng. A variational approach to moving contact line hydrodynamics. *Journal of Fluid Mechanics*, 564:333–360, 2006.

[72] L. C. Evans. *Partial Differential Equations*. American Mathematical Society, Providence, Rhode Island, 1998.

[73] F. Ben Belgacem, Y. Renard, and L. Slimane. A mixed formulation for the signorini problem in nearly incompressible elasticity. *Applied Numerical Mathematics*, 54(1):1–22, 2005.

[74] Roland Glowinski. *Numerical Methods for Nonlinear Variational Problems*. Springer-Verlag, New York, NY, 1984.

[75] E. B. Dussan. The moving contact line: the slip boundary condition. *Journal of Fluid Mechanics*, 77(4):665–684, 1976.

[76] P. A. Durbin. Considerations on the moving contact-line singularity, with applications to frictional drag on a slender drop. *Journal of Fluid Mechanics*, 197:157–169, 1988.

[77] Yulii D. Shikhmurzaev. Singularities at the moving contact line. mathematical, physical and computational aspects.

[78] *Physica D: Nonlinear Phenomena*, 217(2):121 – 133, 2006. V. Girault and P. A. Raviart. *Finite Element Methods for Navier-Stokes Equations: Theory and Algorithms*. Springer-Verlag, Berlin, 1986.

[79] Susanne C. Brenner and L. Ridgway Scott. *The Mathematical Theory of Finite Element Methods*. Springer, New York, NY, 2nd edition, 2002.

[80] Thomas J. R. Hughes. *The Finite Element Method: Linear Static and Dynamic Finite Element Analysis*. Dover Publications, Mineola, NY, 1st edition, 2000.

[81] G. Evans, J. Blackledge, and P. Yardley. *Numerical Methods for Partial Differential Equations*. Springer-Verlag, London, UK, 2000.

[82] Stig Larsson and Vidar Thomée. *Partial Differential Equations with Numerical Methods*. Texts in Applied Mathematics. Springer, New York, NY, 1st edition, 2008.

[83] Eberhard Bänsch. Finite element discretization of the navier-stokes equations with a free capillary surface. *Numerische Mathematik*, 88:203–235, 2001.

[84] Eberhard Bänsch, Pedro Morin, and Ricardo H. Nochetto. A finite element method for surface diffusion: the parametric case. *Journal of Computational Physics*, 203:321–343, 2005.

[85] Gerhard Dziuk. An algorithm for evolutionary surfaces. *Numerische Mathematik*, 58:603–611, 1991.

[86] David Gilbarg and Neil S. Trudinger. *Elliptic Partial Differential Equations of Second Order (Paperback, Reprint of 1998 edition)*. Springer, New York, NY, 2001.

[87] Thierry Aubin. *Nonlinear Analysis on Manifolds. Monge-Ampere Equations*. A Series of Comprehensive Studies in Mathematics. Springer, New York, NY, 1982.

[88] D. Kinderlehrer and G. Stampacchia. *An Introduction to Variational Inequalities and their Applications*. SIAM, Philadelphia, PA, 1987.

[89] Georges Duvaut and Jacques Louis Lions. *Inequalities in Mechanics and Physics*. Springer, New York, NY, 1976.

[90] F. Brezzi and M. Fortin. *Mixed and Hybrid Finite Element Methods*. Springer-Verlag, New York, NY, 1991.

[91] Philippe G. Ciarlet. *The Finite Element Method for Elliptic Problems*. Classics in Applied Mathematics. SIAM, Philadelphia, PA, 2nd edition, 2002. 530 pp. ISBN: 978-0898715149.

[92] J. M. Escobar, G. Montero, R. Montenegro, and Rodríguez. An algebraic method for smoothing surface triangulations on a local parametric space. *International Journal for Numerical Methods in Engineering*, 66(4):740–760, 2006.

[93] Jonathan Richard Shewchuk. Triangle: Engineering a 2D Quality Mesh Generator and Delaunay Triangulator. In Ming C. Lin and Dinesh Manocha, editors, *Applied Computational Geometry: Towards Geometric Engineering*, volume 1148 of *Lecture Notes in Computer Science*, pages 203–222. Springer-Verlag, May 1996. From the First ACM Workshop on Applied Computational Geometry.

[94] S. Osher and R. Fedkiw. *Level Set Methods and Dynamic Implicit Surfaces*. Springer-Verlag, New York, NY, 2003.

[95] David R. Lide, editor. *Handbook of Chemistry and Physics*. CRC Press, Boca Raton, FL, 82nd edition, 2002.

[96] K.-L. Wang and T. B. Jones. Electrowetting dynamics of microfluidic actuation. *Langmuir*, 21(9):4211–4217, 2005.